Performance characterization of a microtrap objective for cold atom experiments

by

Dimitra Cristea

Bachelor thesis in physics
presented to the faculty of physics, mathematics and computer science (FB 08)
at the Johannes Gutenberg-University Mainz
11. April 2023

1. Examiner: Prof. Dr. Patrick Windpassinger
2. Examiner: Prof. Dr. Randolf Pohl

ABSTRACT

This thesis presents the assembly and characterization of a long-working distance objective which consists of five low-cost commercial singlet lenses. This self-assembled objective has a high numerical aperture of NA=0.53 and typical working distance of 31.85 mm making it suitable for Quantum gas experiments. The objective is designed to have diffraction limited performance at the optical trapping wavelength of 1064 nm, which corresponds to a theoretical spatial resolution of 1.45 μm. However, the objective can easily be adapted to optimize performance at shorter or longer wavelengths if needed. In this thesis, performance is evaluated at the design wavelength of 1064 nm to test agreement with simulations. These include measuring the focal spot size and the spatial resolution using a USAF1951 test target. After testing and evaluation, the objective will be installed in the Dipolar Quantum gases experiment for trapping and manipulating Dysprosium atoms.

Declaration of Authorship

I hereby assure, that I wrote this thesis myself. I did not use any other sources than the ones indicated and the quotes are referred to as such.

Mainz, [11.April. 2023] [Signature]

Dimitra Cristea
QOQI
Institute of Physics
Staudingerweg 7
Johannes Gutenberg-University D-55099 Mainz
dcristea@students.uni-mainz.de

Acknowledgements

The research I conducted has given me a newfound appreciation for the complexities and wonders of the physical world. Therefore, I would like to thank Prof. Dr. Patrick Windpassinger for giving me this opportunity to write my thesis in the QOQI research group.

I also want to thank Prof. Dr. Randolf Pohl for kindly agreeing to be my second examiner.

Additionally, I would like to express my gratitude to Ishan Varma and Marvin Proske for their invaluable mentoring. I deeply appreciate their willingness to patiently answer any and all questions, without any hint of judgment, as well as always being motivated and prepared to solve any kind of problem in the lab. It created a safe and comfortable working environment. Thank you for the help in the lab, the poof-reading and all the helpful comments and advises. Also, special thanks to Ishan Varma for entrusting me with his objective and directing me.

I am grateful to Sören Boles, Nivedith K. Anil, and Jean-Pierre Marburger for their assistance in introducing me to new software and helping me resolve any issues I encountered while working with Python. Thanks to them, I developed new computer skills.

Big thanks to Nivedith K. Anil for always being open with my ideas and finding time to help me , even while working on his own thesis.

I also want to thank David Latorre Bastidas, Malavika Unni and Faruk Alexander Sellami for their nice company in the office. Thanks also to Esther del Pino Rosendo, for giving me feedback in presentations.

Last but not least, I want to thank my family and friends for always supporting me through tough times.

Index

1. Introduction **1**

2. Theory **2**
2.1. Numerical aperture . . . 2
2.2. Optical aberrations . . . 2
2.2.1. Chromatic aberration . . . 3
2.2.2. Spherical aberration . . . 4
2.2.3. Coma . . . 4
2.3. Mathematical treatment of laser beams . . . 5
2.4. Gaussian beams . . . 6

3. Setup and methods **11**
3.1. Assembly and alignment of microtrap objective . . . 11
3.2. Knife edge measurement . . . 12
3.3. Focal spot size measurement . . . 14
3.4. Simulation results of aberrations with OpticStudio . . . 15
3.5. Resolution measurement . . . 16

4. Performance evaluation of the microtrap objective **18**
4.1. Setup . . . 18
4.2. Beam profile measurement . . . 19
4.3. Focal spot stability . . . 21
4.4. Focal spot size measurement . . . 24
4.5. Resolution measurement . . . 30

5. Outlook & Discussion **33**

A. Appendix **35**
A.1. Optical objective specifications . . . 35
A.2. Plotting methods and error determination . . . 36
A.3. Assembly and experimental setup pictures . . . 37
A.4. Tables for horizontal measurement . . . 38
A.5. Tables for vertical measurement . . . 45

1. Introduction

Optical trapping of neutral atoms is achieved by using an objective to focus down a laser beam and thereby, create a tight confinement for the atoms at the focus. This technique is referred as optical tweezers and it has ,thanks to Arthur Ashkin and his colleagues, become a powerful tool in diverse fields, allowing for the manipulation and study of microscopic objects like atoms, nanoparticles, human cells and viruses. Optical tweezers have provided researchers a unique tool to explore fundamental questions about the nature of atoms and their interaction with light under different conditions [4].

The QOQI (Experimental Quantum Optics And Quantum Information) research group at the Johannes Gutenberg University is part of the QuCoLiMa (Quantum Cooperativity in Light and Matter) collaborative research center, and focuses on using cold, neutral atoms for quantum optical and quantum information science. One of their projects, deals with light propagation in dipolar media. In this project, we aim to study the interplay between light-induced and magnetic dipole-dipole interactions on the propagation of light and investigate their impact on cooperative effects like sub- or superradiance. Dysprosium (Dy), a rare-earth lanthanide element, is a suitable candidate for studying these effects given that it has the highest ground state magnetic moment of any element in the periodic table (u = 10 Bohr magneton). To this end, we want to create dense and ultracold ensembles of neutral Dysprosium in an Optical Dipole Trap (ODT). The ODT will be generated by focussing down a high power 1064 nm laser beam onto a sample of Dy atoms in a Magneto-Optical Trap (MOT) [9].

The aim of this thesis is to assemble and characterize a high Numerical Aperture (NA) objective, which will be used to create a tight ODT. Understandably, the density of atoms in the ODT depends strongly on the size of the focal region and therefore, the objective has been designed to offer diffraction limited performance and generate the smallest focal spot size possible. The lenses are assembled inside commercial $2''$ lens tubes from Thorlabs. Notably, the performance of the objective strongly depends on the spacing between the individual lenses and therefore, spacer rings are designed and manufactured in the workshop to separate the lenses with high precision.

The performance of the objective is characterized by measuring the profile of the focal region using knife-edge measurement and estimating the spatial resolution using a USAF 1951 resolution test chart. All measurements are performed at the design wavelength of 1064 nm which will be used to create the ODT. Finally, we compare how the results of these measurements compare to simulations and what could be the possible sources of any discrepancies and deviations.

2. Theory

This section will focus on several fundamental concepts in optics, such as numerical aperture, optical aberrations, mathematical treatment of laser beams, and Gaussian beams. These concepts will be useful in discussing the contents of this thesis further on. The information presented here is drawn from two authoritative sources: *Optical Tweezers by Philip H. Jones* and *Microrheology with Optical Tweezers by Manlio Tassieri*. Additionally, all figures used in this section have been created using the software tool *Inkscape* [7].

2.1. Numerical aperture

The range of angles over which an optical system or a lens, can collect or emit light is characterized by Numerical aperture.It is defined as the product of the refraction index **n** of the medium, in which the lens is immersed, and the sine of the angle $\boldsymbol{\theta}$ between the optical axis and the furthest light refraction from the center of the lens, based on geometrical considerations. NA is the result of Abbe's sine condition, required for lenses and optical systems to produce sharp images of off-axis as well as on-axis objects.

$$NA = n \cdot \sin\theta \tag{2.1}$$

Concisely, larger the angle $\boldsymbol{\theta}$, the greater the amount of light captured by the lens, and consequently higher the numerical aperture.It can be shown that an optical system with a higher NA can, in principle, produce higher resolution images. That is to say, NA determines the reoslving power of an optical system. NA is the most convenient way to describe the lens aperture since it is directly proportional to the light gathering ability of an optical system. For more complex optical systems that deviate significantly from paraxial conditions, more advanced models are being used to determine the numerical aperture. These models are not going to be discussed in this thesis, since all optical systems used in this thesis fulfill Abbe's sine condition.

2.2. Optical aberrations

Optical aberrations refer to the imperfections or any deviations from the ideal "diffractionlimited" imaging performance of the system.

The aim of imaging, in the ideal case, through an aptical system can be defined as follows: *the system must capture all light radiating in every direction from a given* *point on the object and converge it to the optimal image point* [2]. This would also require the beam of light originating from the object point to traverse the lens at any angle and ultimately reach the corresponding image point. Nevertheless, various types of optical aberrations can arise in this process, such as chromatic aberration, spherical aberration, tilt, field distortion, coma, and astigmatism. This thesis will focus primarily on three types of optical aberrations: chromatic aberration, spherical aberration, and coma. These aberrations are discussed due to their significant impact they have on image quality and their prevalence in real-world optical systems [1].

2.2.1. Chromatic aberration

Chromatic aberration occurs when a lens or an optical system refracts different wavelengths of light differently. Chromatic aberrations are divided into two subtypes: axial and lateral color, also referred as longitudinal and transverse, respectively. Both types of chromatic aberrations can be particularly noticeable in lenses with a large aperture or high magnification, and can significantly impact the overall image quality. Axial chromatic aberration is caused by the difference in focal length of the lens for different wavelengths of light along the optical axis. Whereas, lateral chromatic aberration is the result of different wavelengths of light refracted by a lens at different angle, causing them to be displaced laterally from each other in the final image.

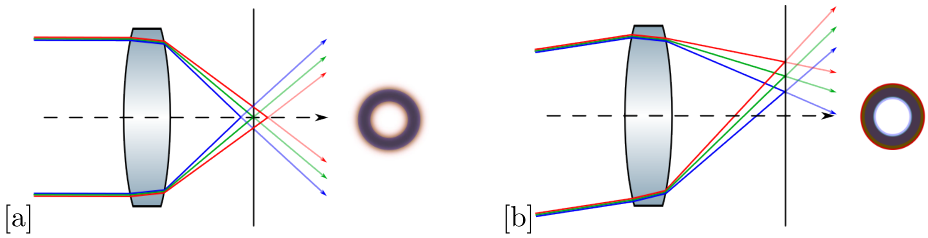

Fig. 2.1: Comparison of [a] axial and [b] lateral chromatic aberration.

The focal length for a thin lens with axial chromatic aberration is given by:

$$\frac{1}{f_i} = (n_i - 1)\,\frac{R_{i2} - R_{i1}}{R_{i2} \cdot R_{i1}}, \tag{2.2}$$

where n_i is the *refractive index*, R_{i1} and R_{i2} the curvature radii of the front and back surfaces of the i-th lens. It is important to note that the refractive index, $n(\lambda)$, of a lens material is dependent on the wavelength, λ, of the light passing through it. Consequently, the focal length of the lens also changes with the wavelength of the light [8].

This *Lens maker's formula* is a mathematical expression that takes in physical parameters, such as the radius of curvature and refractive index of a lens surface, to determine its focal length. This formula can effectively calculate the focal length of a lens that suffers from axial chromatic aberration. However, lateral chromatic aberration is not depended on these physical parameters but rather on the angle of incidence and magnification of the lens. Thus, it's important to note that the "Lens maker's formula" cannot be applied to calculate lateral chromatic aberration.

2.2.2. Spherical aberration

Spherical aberrations occur when light rays passing through a lens are refracted differently depending on their distance from the center of the lens. This results in light rays that strike the lens near the edge being deflected differently than those that strike the lens nearer to the center. Similar to chromatic aberration, spherical aberration can also be categorized into two subtypes: axial and lateral. Spherical aberrations can be classified as either positive or negative. A positive spherical aberration occurs when peripheral rays are bent to much, and a negative spherical aberration occurs when peripheral rays are not bent enough [2].

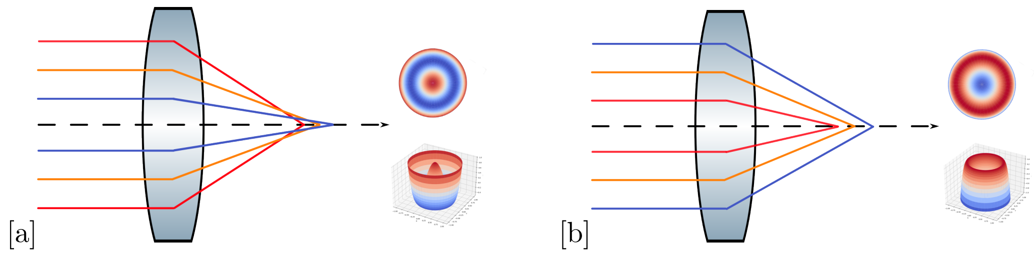

Fig. 2.2: Sketch representing [a] positive and [b] negative spherical aberration.

2.2.3. Coma

Coma aberration, also known as comatic aberration, refers to the case where the magnification varies across the entrance pupil, resulting in off-axis objects appearing comet-like. In other words, skew rays passing through a lens fail to behave like meridional rays.

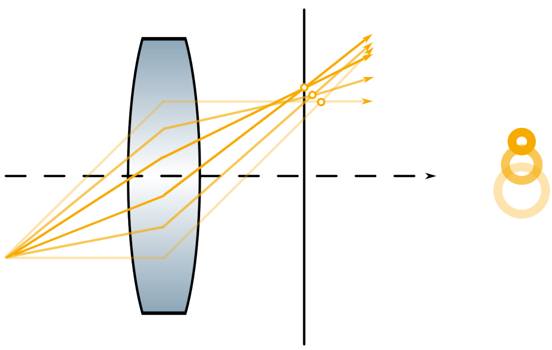

Fig. 2.3: Comatic aberration forming a comet shaped image.

Compared to spherical aberration, which results from the failure of meridional rays to obey the paraxial approximation, coma arises from the inability of skew rays to behave like meridional rays.

2.3. Mathematical treatment of laser beams

The wave equation is a partial differential equation that characterizes the behaviour of waves in a medium. When a wave travels through a medium, it causes the material to experience deformation and stress. To solve the wave equation, it is necessary to know the displacement and stress at any point along the beam, as functions of both time and position. For this purpose, the wave equation can be obtained from the Maxwell equations. Assuming no free charge or free current ($\rho_f = 0; J_f = 0$).

$$\nabla \cdot \mathbf{E} = 0, \tag{2.3}$$

$$\nabla \cdot \mathbf{H} = 0, \tag{2.4}$$

$$\nabla^2 \times \mathbf{E} = -\mu_0 \mu_r \frac{\partial \mathbf{H}}{\partial t}, \tag{2.5}$$

$$\nabla^2 \times \mathbf{H} = \epsilon_0 \epsilon_r \frac{\partial \mathbf{H}}{\partial t}. \tag{2.6}$$

Taking the curl of the eq 2.5 and substituting in Maxwell eq 2.3 and eq 2.6 to solve for $\mathbf{E}$, we get:

$$\nabla^2 \mathbf{E} - \epsilon_0 \mu_0 \epsilon_r \mu_r \frac{\partial^2 \mathbf{E}}{\partial^2 t} = 0 \tag{2.7}$$

$$\Rightarrow \nabla^2 \mathbf{E} - \frac{n^2}{c^2} \frac{\partial^2 \mathbf{E}}{\partial^2 t} = 0, \tag{2.8}$$

where $c^2 = 1/\epsilon_0 \mu_0$ is the speed of light and $n^2 = \epsilon_r \mu_r$ is the refractive index of the medium. Using the expression for wave velocity v, $v^2 = \frac{c^2}{n^2}$ we have the equation,

$$\nabla^2 \mathbf{E} - \frac{1}{v^2} \frac{\partial^2 \mathbf{E}}{\partial^2 t} = 0. \tag{2.9}$$

Laser beams are coherent optical beams with a finite transverse extent. This finite extent or spatial confinement is achieved by ensuring that the solutions to the wave equation, which determine the behavior of the beam, decay exponentially transverse to the direction of propagation, in our case in the z-direction. One method of determining the shape of these confined beams involves using the *slowly varying envelope approximation*. This approximation involves expressing the field as a product of monochromatic carrier plane wave and an envelope varies more gradually in the transverse direction compared to the wavelength of the wave in the longitudinal direction. This approximation allows us to more accurately describe real life laser beams and take into account their finite transverse extent. This leads us to the paraxial wave equation. To derive the paraxial wave equation, we begin by substituting a plane wave solution for eq 2.10 that propagates in the z-direction into eq 2.9.

$$\mathbf{E}(\mathbf{r}, t) = \mathbf{E}_0 e^{i(\mathbf{k}\cdot\mathbf{z}-\omega t)} \tag{2.10}$$

Noting $k^2 = \frac{\omega^2 n^2}{c^2}$ and using $\nabla_\perp^2 \equiv \frac{\partial^2}{\partial x^2} + \frac{\partial^2}{\partial x^2}$ we get,

$$\nabla_\perp^2 E_0 + \frac{\partial^2 E_0}{\partial z^2} + 2ik\frac{\partial E_0}{\partial z} - k^2 E_0 + \frac{\omega^2}{v^2} E_0 = 0 \tag{2.11}$$

Using the slowly varying envelope approximation, where $\mathbf{E}_0$ is the envelope. We can neglect one of the terms.

$$\left|\frac{\partial^2 E_0}{\partial z^2}\right| \ll \left|2ik\frac{\partial E_0}{\partial z}\right| \ll \left|k^2 E_0\right| \tag{2.12}$$

Therefore the expression can be written in the following way, taking additionally into account $k^2 = \frac{\omega^2 n^2}{c^2} = \frac{\omega^2}{v^2}$.

$$\nabla_\perp^2 E_0 + 2ik\frac{\partial E_0}{\partial z} = 0 \tag{2.13}$$

This expression is known as the paraxial wave equation. Although it is not an accurate description for beams under strong focusing conditions, it is often used as a simplified approximation for practical reasons. In the remaining section, we will discuss laser beams in within this approximation.

2.4. Gaussian beams

Gaussian beams are the most commonly used type of laser beams and are also used in this thesis. They are characterized by a bell-shaped intensity profile, as shown in Figure 2.4. In other words, a profile that has highest intensity at the center of the beam which falls off towards the edges. Another property of a Gaussian beam, is beam divergence, which relates the size of the beam with the propagation distance.

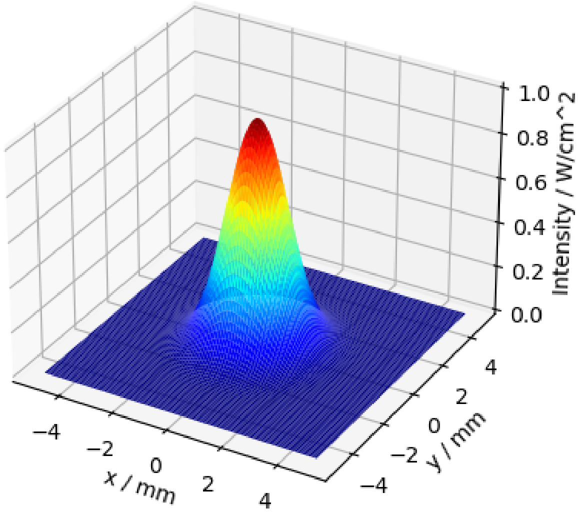

Fig. 2.4: Gaussian beam profile, where red indicates high intensity and blue low intensity.

Additionally, it exhibits the least angular divergence and can be focused to achieve the smallest spot size.

We will now attempt to derive the mathematical expression which describes a Gaussian beam by assuming a trial solution of the form,

$$E_0(r, z) = A(z)e^{\frac{ikr^2}{2q(z)}} \tag{2.14}$$

where A(z) represents the amplitude and q(z) determines the properties of the Gaussian beam as it propagates. To determine the form of these to variables, we substitute eq 2.14 into the paraxial wave solution eq 2.13. This would give:

$$\frac{2ik}{q} - \frac{k^2r^2}{q^2} + 2ik\left(\frac{1}{A}\frac{dA}{dz} - \frac{ikr^2}{2q^2}\frac{dq}{dz}\right) = 0 \tag{2.15}$$

Equating terms in like powers of r, leads us to the following relations:

$$\frac{1}{A}\frac{dA}{dz} = -\frac{1}{q}, \tag{2.16}$$

$$\frac{dq}{dz} = 1 \quad \Rightarrow \quad q = q_0 + z \tag{2.17}$$

Integrating now the equation eq 2.16, we get:

$$A(z) = \frac{q_0}{q_0 + z}. \tag{2.18}$$

Substituting for A(z) in the trial beam solution 2.13, we get:

$$E_0(r, z) = \frac{q_0}{q_0 + z} e^{\frac{ikr^2}{2q(z)}} \tag{2.19}$$

For large propagation distances, we can use the approximation $z \to \infty$, which leads to the limit $q \to z$. Eq 2.10 can then be written as:

$$E(r, z) = E_0(r, z) e^{i(kz - \omega t)} = \frac{q_0}{z} e^{\frac{ikr^2}{2z}} e^{i(kz - \omega t)} \tag{2.20}$$

$$\Rightarrow \quad E(r, z) = \frac{q_0}{z} e^{ik(z + \frac{r^2}{2z})} e^{-i\omega t} \tag{2.21}$$

To have a more intuitive understanding of $q(z)$ and $A(z)$, we can compare equation eq 2.21 to the expected wave equation for very large propagation distances $z \to \infty$. In this case, the wave should look like a spherical wave for a point source, which can be expressed as:

$$E(r, z) = \frac{e^{ikR}}{R} e^{-\omega t} \tag{2.22}$$

where $R = \sqrt{r^2 + z^2}$ is the radius of curvature in the phase front. Since $R \gg r$, we can expand R as:

$$R \approx z + \frac{r^2}{2z} + ... \tag{2.23}$$

$$\frac{1}{R} \approx \frac{1}{z} - \frac{r^2}{2z^3} + ... \tag{2.24}$$

Therefore, substituting for $1/R$ into eq 2.22 and taking the limit of $z \gg r$, leads us to the paraxial-spherical wave equation:

$$E(r,z) = \frac{1}{z} e^{ik(z - \frac{r^2}{2z})} e^{-i\omega t} \tag{2.25}$$

It is clear, that the result is equivalent to eq 2.21 And hence, q is the radius of curvature of the phase front near the z-axis. Examining eq 2.19, we conclude that q must be complex. This leads to the following expression for the electric field associated with the beam:

$$E(r,z) = A(z) e^{ik[z + \frac{r^2}{2z} Re\left(\frac{1}{q(z)}\right)]} e^{\frac{-kr^2}{2} Im\left(\frac{1}{q(z)}\right)} e^{-i\omega t} \tag{2.26}$$

Here, the second exponential expression represents a Gaussian function with a width of $w(z)$. In simpler terms, we can express it as follows:

$$e^{\frac{-kr^2}{2} Im\left(\frac{1}{q(z)}\right)} = e^{\frac{-r^2}{w(z)^2}} \tag{2.27}$$

where

$$w(z) = \left[\frac{k}{2} Im\left(\frac{1}{q(z)}\right)\right]^{-1/2} \tag{2.28}$$

Note that $Im\left(\frac{1}{q(z)}\right)$ decreases away from z=0, and thus $w(z)$ has a minima at z=0. Therefore, w_0 is the *beam waist*. From Eq. 2.20 we can also conclude that surfaces of constant phase must obey:

$$z + \frac{r^2}{2z} Re\left(\frac{1}{q(z)}\right) = const. \tag{2.29}$$

Taking into account that away from $z = 0$, $Re\left(\frac{1}{q}\right)$ must be non-zero and the phase fronts nearly parabolic. We define the radius of curvature of the wavefront, such that:

$$\frac{1}{R(z)} = Re\left(\frac{1}{q(z)}\right) \tag{2.30}$$

This leads to the general expression for the complex beam parameter, q:

$$\frac{1}{q(z)} = \frac{1}{R(z)} + \frac{2i}{kw(z^2)} \tag{2.31}$$

where $w(z)$ is a measure of the decrease of the field amplitude, E0, with the distance from the axis, which is Gaussian in form. The minimum diameter of the Gaussian is $2w_0$ and occurs at the beam waist where the phase front is plane.
By using equations eq 2.17 and eq 2.31, and equating the real and imaginary components, we can derive the explicit form of beam width and wavefront curvature as a function of z..

$$w^2(z) = w_0^2 \left[1 + \left(\frac{2z}{kw_0}\right)^2\right], \tag{2.32}$$

$$R(z) = z\left[1 + \left(\frac{kw_0}{2z}\right)^2\right]. \tag{2.33}$$

Lastly, it's worth mentioning that $A(z)$ experiences a phase shift of π as it propagates from a large negative value of z, passes through the beam waist, and reaches a large positive value of z. This particular distance is commonly referred to as the *Rayleigh length or Rayleigh range*, and is given by $z_R = kw_0^2/2$.
The transverse intensity profile of the *Gaussian* beam takes the form:

$$I(\mathbf{r}, z) = |A(\mathbf{r}, z)|\, e^{\left(\frac{-2r^2}{w(z)^2}\right)} \tag{2.34}$$

where A($\mathbf{r}$) is the amplitude on the z-axis and has dimensions of the field, while the beam width is determined by $w(z)$. Both of these parameters undergo changes due to diffraction. The radial distance from the axis of the beam, denoted as r, is defined as $r = \sqrt{x^2 + y^2}$. An intuitive visual representation of the parameters are shown in the Figure 2.5 below. From the Figure 2.5 we can conclude that at large distances ($z \gg z_R$), w increases linearly with z; hence the beam *divergence angle* θ, given in radians, can be defined, due to diffraction, as

$$\theta = \lim_{z\to\infty} \frac{w(z)}{z} \simeq \frac{w_0}{z_R} \tag{2.35}$$

The following Figure 2.5 shows the parameters presented in this section.

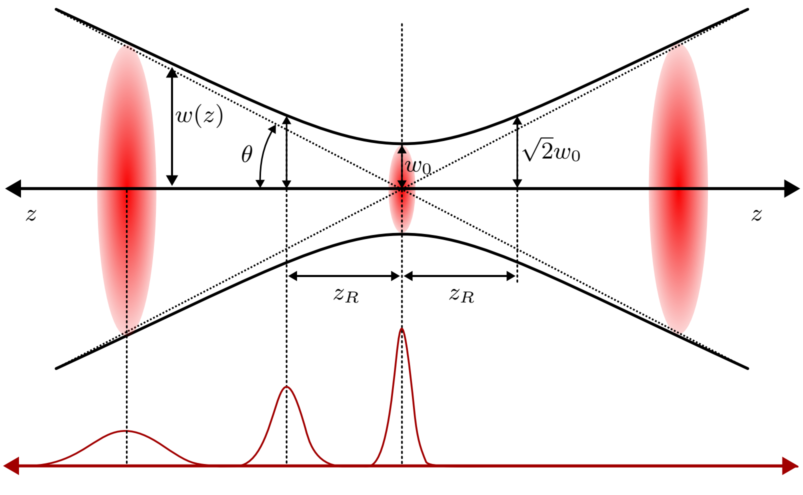

Fig. 2.5: Useful beam parameters. Evolution of the radius of the Gaussian beam along the z-axis as a function of the beam waist w_0, the Rayleigh range z_R, and the divergence angle θ. The lower part shows intensity projections at three different positions of a Gaussian beam. The projection at $z = 0$ has the narrowest waist.

3. Setup and methods

In this section, the methods and experimental setups used in this thesis are presented, including the assembly of the microtrap objective. These techniques were essential for characterizing the optical properties of the optical system and comparing experimentally obtained data with simulations. Goal in presenting these methods is to provide a comprehensive understanding of the techniques used in this study and their significance in achieving precise measurements.

3.1. Assembly and alignment of microtrap objective

This thesis primarily discusses the design, assembly and characterization of a multi-lens objective (Fig: 3.1) that focuses a laser beam into a tightly confined spot used for creating optical microtraps. The system was designed by combining five different commercial lenses, and optimizing the distances between them to minimize aberrations and misalignment. To ensure the lenses were correctly spaced, spacer rings were designed and installed in the system.

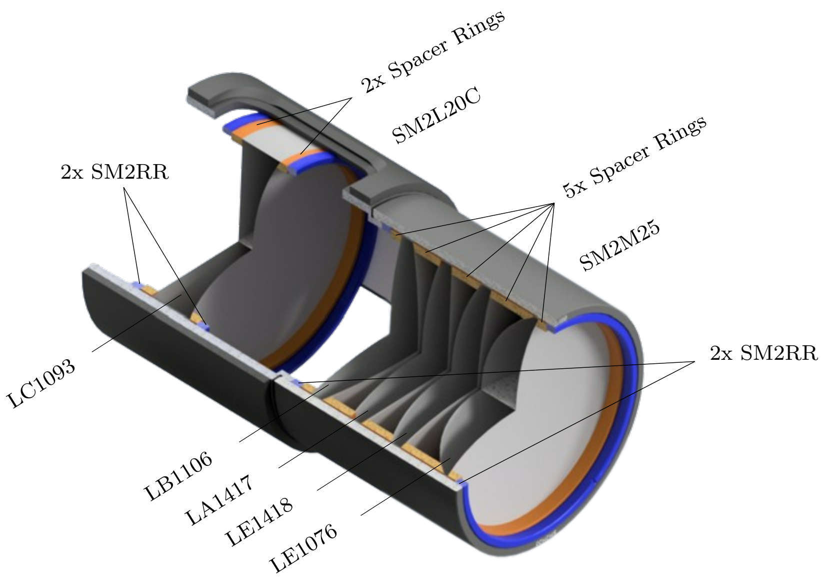

Fig. 3.1: Schematic of the microtrap objective.

Achieving stable and precise alignments is crucial for sensitive optical measurements. In our experiment, a laser with a wavelength of 1064nm is used, which falls in the near-infrared region of the electromagnetic spectrum. Given that infrared radiation is invisible to the human eye, aligning the beam through the optical axis of the system is challenging. To overcome this, we used a laser beam in the visible region (626 nm) as a reference and align it centrally through the optical system. Following this, the 1064 nm beam was overlapped onto the visible beam to acheive an indirect alignment, as shown in the Figure 3.2 below. Following this, a beam profiler is placed at two different points to further refine the alignment.

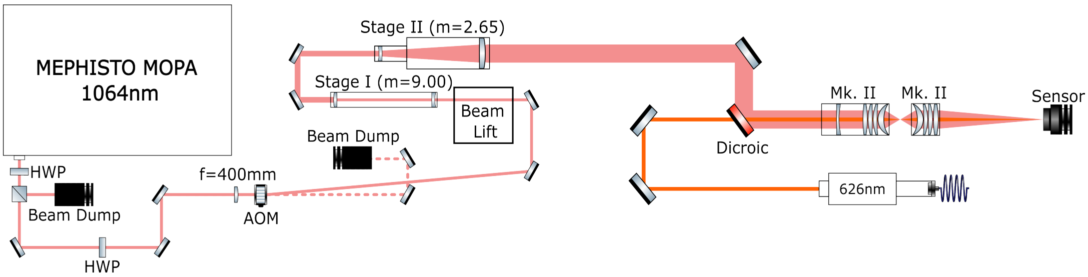

Fig. 3.2: Schematic of the experimental setup for focal spot measurement of the 1064 nm laser beam. 626 nm laser beam is used as a reference for aligning the 1064 nm beam.

3.2. Knife edge measurement

One commonly used method for characterizing the size of laser beams is through *knife edge measurement*. We used this technique to measure the size of the beam close to the focal plane. This method requires a sharp knife edge or blade, a high precision piezoelement connected to a translation stage capable of moving in all three directions, and a power sensor. Here, the knife edge is placed in the path of the laser beam and moved slowly across the beam using the piezoelement translation stage. The sensor measures the laser power as the knife edge passes through the beam, allowing for the determination of the beam profile and size. Therefore, this technique is particularly useful for measuring the size and intensity of the focal point.

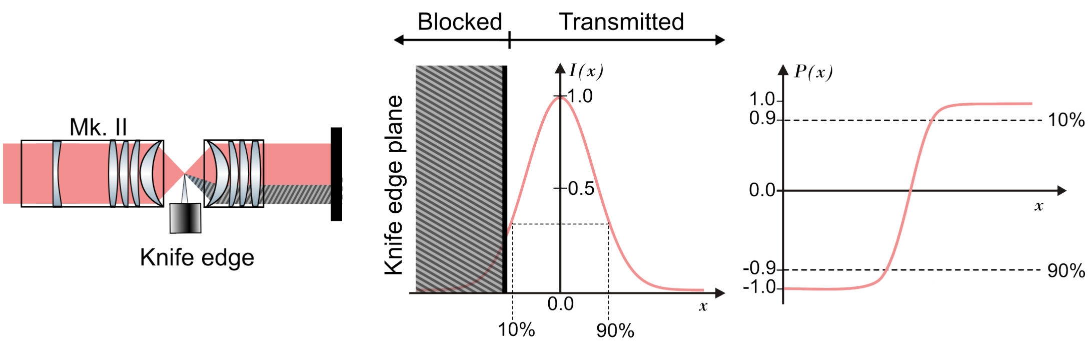

Fig. 3.3: Example scheme of measured signal from knife edge measurement.

The data obtained through knife edge measurement can be analysed with the help of the *error function.* The error function is an essential mathematical tool for modeling the intensity distribution of the laser beam. For a Gaussian beam, the recorded intensity profile in the x-direction corresponds to an error function of the following form [5]:

$$I(x,z) = \frac{P(x)}{A} = \frac{P_0}{2A}\left[1 + erf\left(\frac{\sqrt{2}x}{w_0}\right)\right], \tag{3.1}$$

where $P_0 = (\pi/2)w_0^2 I_0$, x is the position of the knife edge perpendicular to the beam's propagation and $erf(z)$ is the Gaussian error function defined as

$$erf(z) = \frac{2}{\sqrt{\pi}}\int_0^z e^{-t^2}dt. \tag{3.2}$$

Thus, the error function can also be used to fit the experimental data obtained through knife edge measurement to a theoretical model, allowing for the determination of the beam size. Data points can then be fitted with the fitting function:

$$I(x,z;\alpha,x_0,w,c) = \alpha \cdot \left[1 + erf\left(\frac{\sqrt{2}(x-x_0)}{w(z)}\right)\right] + c, \tag{3.3}$$

where $\alpha = P_0/2A$. In addition, two other parameters were added in the fit function, parameter x_0 and the offset c. The inclusion of the parameter x_0 enables a shift of the function along the x-axis. This adjustment is required due to the inability to set the center of the beam as the zero position on the piezoelement. The purpose of the offset c is to allow for a possible power offset on the power sensor. Lastly, $w(z)$ is the beam radius as a function of the propagation distance z.

3.3. Focal spot size measurement

To find the focus of a Gaussian beam, one typically measures the beam radii $w(z)$ at various positions z around the focus. However, a rough estimation of the position of the focus can be approached through the following methods. One useful method involves observing the laser beam's cross-section on a viewer card and examining the shadow cast by the cutting edge. If the shadow appears on the same side as the cutting edge, it is located behind the focus. Conversely, if the shadow appears on the opposite side, the cutting edge is in front of the focus. This effect is illustrated in Figure 3.5.

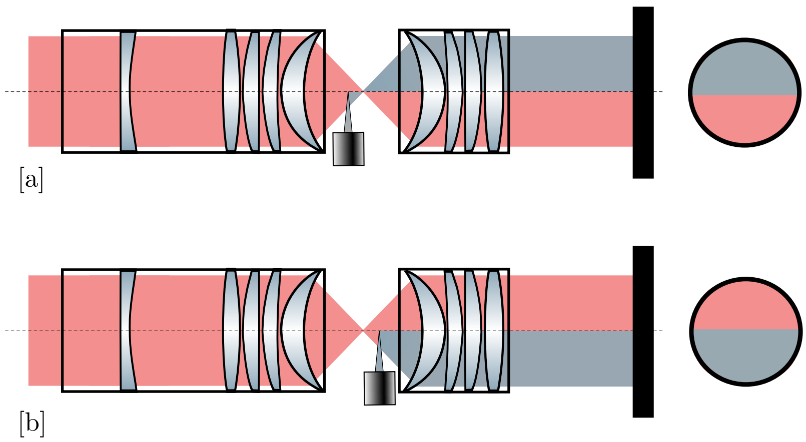

Fig. 3.4: Visual representation of a knife edge passing through a beam close to the focus. If the knife edge is before the focus, the shadow appears on the opposite side (a). However, if it is located after the focus, the shadow forms on the same side (b).

As the cutting edge approaches the focus, the shadow becomes more difficult to observe. At the focus position, the beam disappears almost instantaneously, making it challenging to determine the shadow's location. Nevertheless, this approach provides a rough estimate of the cutting edge's position relative to the focus.

Another approach involves placing a piece of paper between the two objectives and observing a spark, which indicates the beam focus. For an invisible beam, such as the 1064 nm beam, this method may be more practical and efficient. Observing the beam directly on a viewer card is difficult,, especially at low powers.

After approximately finding the position of the focal point, the knife edge can then be placed either in front or behind the focal point and moved,in small steps, towards the focal point and then through it to have a profile of the beam close to the focal plane. The obtained beam radii from each step, $w(z)$, can be then plotted against their corresponding z positions. Their behavior follows eq 3.3, which describes the dependence of the beam radius on the axial position z. We then fit the collected data using the following function [5]:

$$w(z; w_0, z_0) = w_0 \sqrt{1 + \left(\frac{z - z_0}{z_R}\right)} \tag{3.4}$$

where w_0 is the sought fit parameter, which represents the minimum beam waist, z_R is the *Rayleigh range* and z_0 is the offset. However, laser beams used in real life are not always perfectly gaussian and may have aberrations or imperfections in their profile. The fitting function 3.4 must then be modified to also fit beams which are not perfectly gaussian. This is done by introducing the *beam quality factor* M^2. The modified fit function takes the form:

$$w(z; M^2, w_0, z_0) = w_0 \sqrt{M^2 + M^2 \left(\frac{z - z_0}{z_R}\right)} \tag{3.5}$$

The beam quality factor M^2 is a measure of the quality of a laser beam. It is a dimensionless quantity that describes how closely a laser beam resembles an ideal Gaussian beam. Mathemaically, M^2 is given by the expression [10]:

$$M^2 = \frac{\pi}{2} \frac{w_0 \cdot \theta}{\lambda} \tag{3.6}$$

where θ is the divergence angle mentioned in figure 2.6. An ideal Gaussian beam has an M^2 value of 1. In contrast, a beam with $M^2 > 1$ indicates that it deviates from the ideal Gaussian beam and has a more complex profile, while with $M^2 < 1$ it indicates that the beam is divergent and has a lower quality.

3.4. Simulation results of aberrations with OpticStudio

The seidel aberrations diagram from Zemax, presents a graphical representation of the seven seidel coefficients for each surface of the lens. It also displays the total sum of each seidel coefficient in the focal plane, specifically for a selected wavelength. These seidel coefficients include spherical aberration, coma, astigmatism, field curvature, distortion, axial color, and lateral color.

The following Figure 3.5 shows the corresponding seidel diagram of the objective for the wavelength $\lambda = 1064$ nm . When focusing a laser beam through a glass window, spherical aberration is the primary aberration that occurs. The objective is designed in a way that the spherical aberration contributions from each surface cancel each other out. This becomes evident upon observing the total sum of each seidel coefficient in the focal plane, which, in this case, implies that there is minimum to no spherical aberration resulting from the objective.

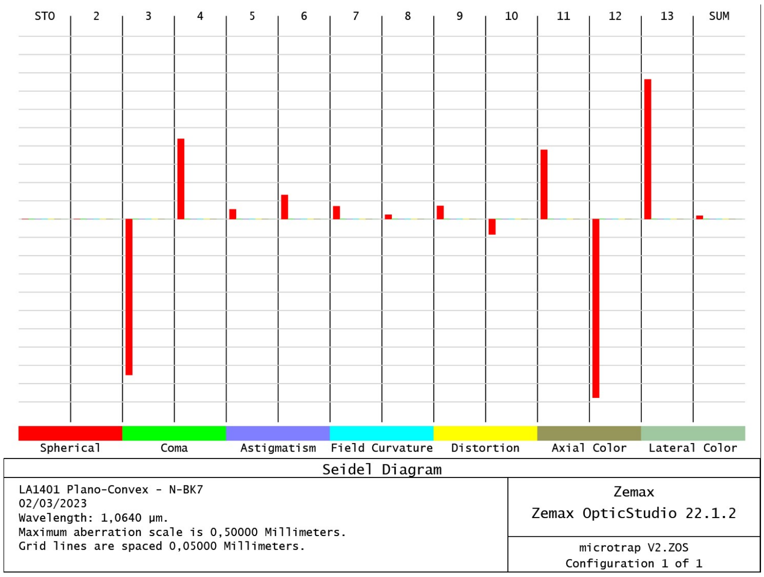

Fig. 3.5: Seidel diagram of aberrration results from Zemax

3.5. Resolution measurement

Another common method of characterizing the performance of an objective is by measuring its resolution. This is important because the objective's resolution determines how closely the atoms can be trapped, and the accuracy with which they can be positioned and manipulated. For this purpose, a commonly used test target known as the USAF 1951 target [1] was used to measure the resolution. The USAF 1951 target consists of multiple sets of horizontal and vertical lines in various sizes, enabling a simultaneous horizontal and vertical resolution measurement at discrete spatial frequencies (line pairs per millimeter) in the object plane.

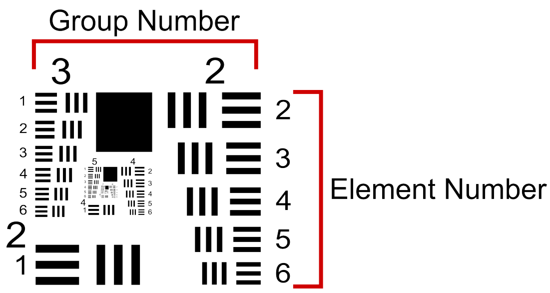

Fig. 3.6: USAF 1951 target.

As shown in the Figure 3.5 above, each element is assigned a number from 1 to 6 and has a unique set of widths and spacings. Groups of six consecutive elements

[1] Erdmund 2" x 2" Negative, USAF 1951 High Resolution Target

are identified with a number ranging from -2 to 7, which can be positive, negative, or zero. These group and element numbers are then used together to determine the spatial frequency (in line pairs per millimeter or lp/mm). The resolution (defined as the number of resolvable line pairs per millimeter), is given as [6]:

$$R[lp/mm] = 2^{G+\frac{E-1}{6}} \tag{3.7}$$

where R is resolution in lp/mm, G is group number and E is the element number. A visual representation of the experimental setup for measuring the resolution is shown in the figure below. In this setup, an achromatic doublet lens is attached to the microtrap objective to image the target onto a camera sensor. The image of the target on the camera/beam profiler is monitored on a PC directly.

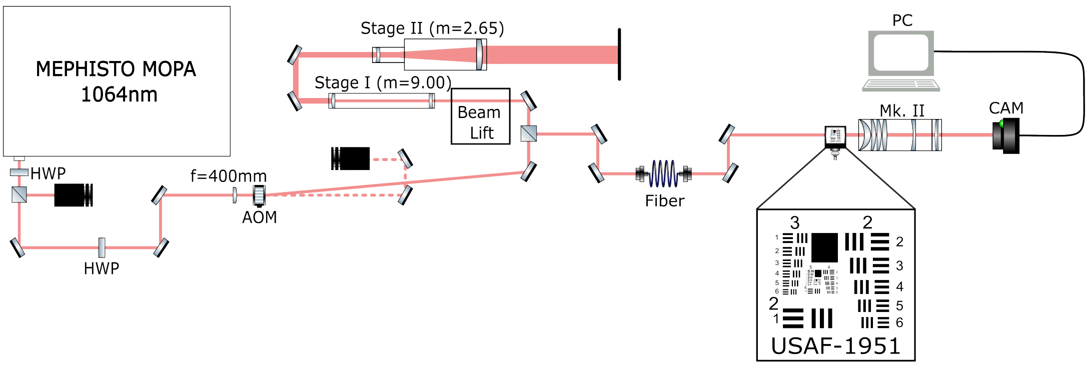

Fig. 3.7: Setup for resolution measurement. The USAF 1951 target is placed at the focal plane of the micro objective and the camera is placed at the focus of the achromat lens.

4. Performance evaluation of the microtrap objective

This section focuses on evaluating the performance of the micro-objective. The experimental setup used for this purpose is presented in the following section.. Therefore, this section begins by presenting the experimental setup, including the beam profile and size utilized in the experiment. Additionally, measurements to estimate the beam size and profile for the incident beam and the focussed down beam close to the beam waist are presented in the following sections. Finally, the resolution of the objective will be determined by using the USAF 1951 resolution chart.

4.1. Setup

In this experiment, a high-powered laser [1] with a wavelength of $\lambda = 1064$nm was used. The output of the laser is divided between the experiment and a beam dump using a half waveplate (HWP) and a plate beamsplitter (PBS) arrangement for flexibility. A HWP optimizes the polarization of the beam going into the experiment for optimal coupling into an Acousto-optic modulator (AOM).

The 0th order diffraction beam from the AOM goes into a beam dump whereas the first order is directed through 2 magnification stages (stage 1 and stage 2)for enlarging the beam. Stage 1 has a magnification factor of m = 9 and stage 2 has a magnification factor of m = 2.65. After magnification, the beam size is close to 25 mm. A large beam is better suited for generating a tight and deep optical dipole trap.

The beam is then focused down using the objective and an improvised multi lens system is placed after the focus to collect light and direct it onto a power sensor.A knife-edge mounted on a *piezoelectric element*, or *piezoelement*, is used to perform knife-edge measurements for evaluating the beam profile and size.A combination of three piezoelements creates a 3 dimensional translation stages which can be used to move the knife edge into the beam with sub-micrometer precision. The knife-edge is placed close to the focus of the beam, as shown in Figure 4.1.

[1] Coherent Mephisto MOPA, Ultra-Narrow Linewidth High-Power CW DPSS Laser

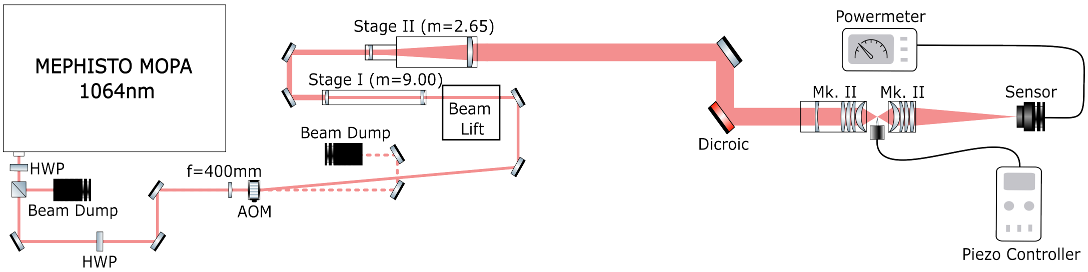

Fig. 4.1: Knife-edge measurement using a pizeoelement mounted knife-edge.

4.2. Beam profile measurement

The objective under consideration has been designed for operation with collimated gaussian laser beams. Therefore, it is important to study the beam profile of the incident beam and determine how close it is to an ideal gaussian beam. A beam that is, for e.g., elliptical or has a non-uniform intensity distribution would lead to a decrease in performance of the objective and consequently, impact the optical microtrap generated using the objective. Therefore, an image of the beam profile was captured using a beam profiler camera [2] directly before Stage II. This position was chosen because the beam size after Stage II is too large for the camera sensor to accomodate.

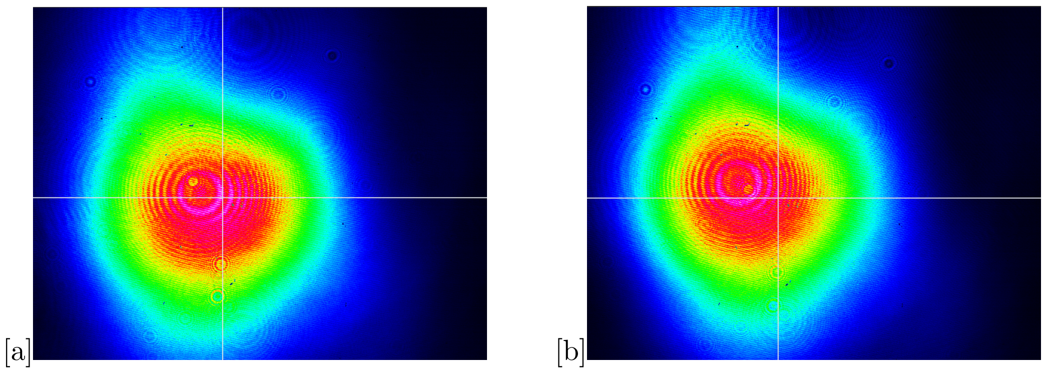

Fig. 4.2: Beam profile of the 1064 nm laser at [a] 800mW and [b] 200mW.

Based on the images obtained, It can be observed that the beam did not exhibit a perfectly Gaussian profile, but rather a close approximation to it. Additionally, a knife-edge measurement was performed directly before the objective in both, horizontal and vertical directions to more accurately determine the size of the beam. Instead of using a piezoelectric element, a manual translation stage with micrometer precision was utilized for this measurement since despite having a lower resolution, they have a higher range which is more important here. Using the error function as described in section 3.5, we fit the data obtained from these knife edge measurements to extract

[2]Edmund Optics Beam Profiler 4M

the σ width and error values of each measurement. Figures 4.3 and 4.4 show a plot of the data points and the fit for the horizontal and vertical directions respectively.

The horizontal measurement was performed by moving the a vertical knife edge (with respect to the optical table) horizontally across the beam. The procedure is repeated three times to account for statistical variations. As shown in Figure 4.3, there is minimal variation among the data points from the three measurements. This indicates that the beam remains stable on the horizontal axis and that the horizontal beam waist is consistent. Averaging the three σ values obtained from the measurements, the average radius of the beam was found to be $4\sigma = 28.90 \pm 0.18$ mm. This is an acceptable beam size to work with when using 2-inch optics.

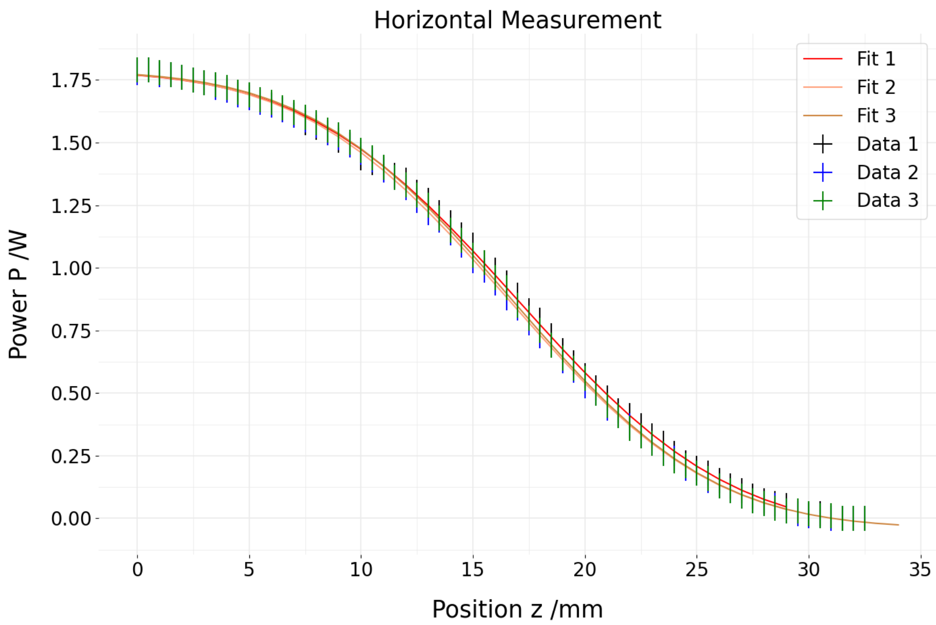

Fig. 4.3: Plot of the power P as a function of the position x of the knife edge for the incident beam $\lambda = 1064$ nm. Eq 3.3 was used to fit the data. The resulting sigma widths are; $\sigma_1 = 7.41 \pm 0.06$ μm, $\sigma_2 = 7.18 \pm 0.03$ μm, $\sigma_3 = 7.07 \pm 0.04$ μm

For the vertical measurement, the knife edge was placed horizontally with respect to the optical table's surface. However, unlike the horizontal measurement, there were noticable variations among the three data sets as depicted in Figure 4.4. These results suggest that the beam was not stable along the vertical axis. By averaging the three σ values obtained from the vertical measurement, the average beam radius was found to be $4\sigma = 20.46 \pm 0.17$ mm.

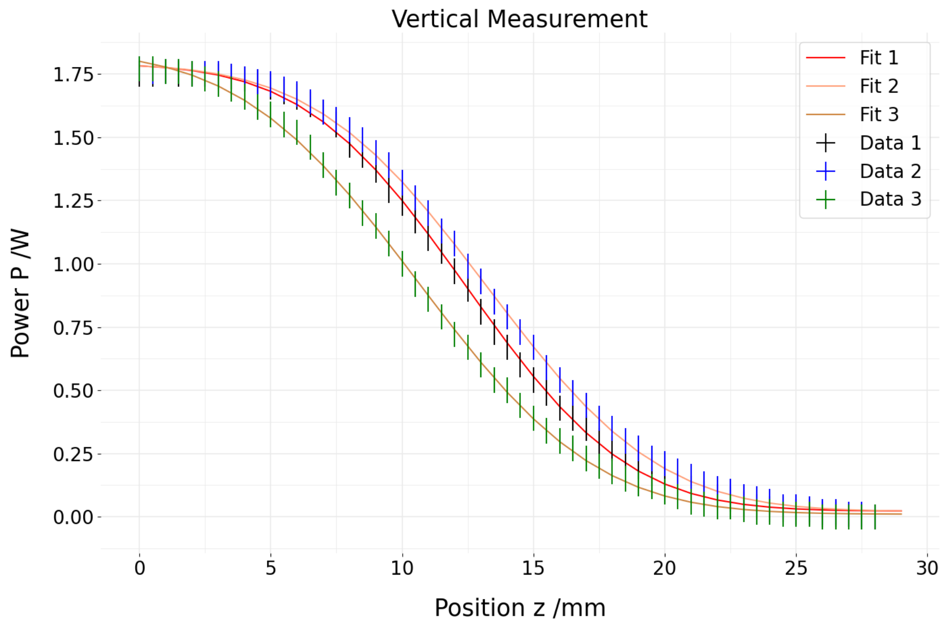

Fig. 4.4: Plot of the power P as a function of the position x of the knife edge for the incident beam $\lambda = 1064$nm. Eq 3.3 was used to fit the data. The resulting sigma widths are; $\sigma_1 = 4.86 \pm 0.05$ μm, $\sigma_2 = 5.15 \pm 0.03$ μm, $\sigma_3 = 5.33 \pm 0.04$ μm

Based on these results, it can be concluded that the beam does not exhibit a perfectly Gaussian profile, but rather a close approximation to it. These measurements confirm that the beam is elliptical in shape, and therefore it can have a negative effect on the performance of the microtrap. The ellipticity of the beam can lead to a non-uniform trap depth, which can affect the atom trapping efficiency of the microtrap.

Tab. 4.1: Size of the beam with a wavelength of $\lambda = 1064$ nm.

	Horizontal	Vertical
4σ [mm]	28.90 ± 0.18	20.46 ± 0.17

4.3. Focal spot stability

To investigate the effects of the statistical variations in the beam size as seen in the previous section on the focal point of the microtrap objective, we perform further measurements. In this section, 10-90 knife edge measurement method is used at different distances from the focus. The 10-90 method approximates the size of a beam by noting the positions of the knife-edge at which 10% and 90% of the total beam power is passing through. This distance is defined as the 10-90 size of the beam. This method was used for both the horizontal and vertical axes to observe the stability of the focal point for both axes.

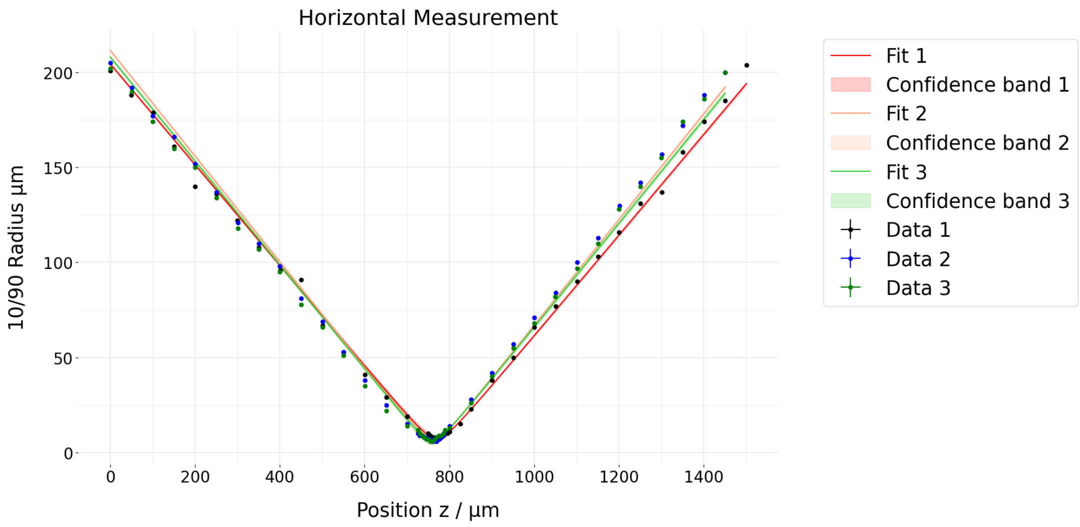

)

Fig. 4.5: Plot of the 10/90 radius as a function of the position z of the knife edge for the incident beam $\lambda = 1064$nm. Eq 3.5 was used to fit the data. The resulting radii of the focal spot are; $r_1 = 7.45 \pm 1.28$ μm, $r_2 = 5.80 \pm 1.51$ μm, $r_3 = 6.20 \pm 1.72$ μm.

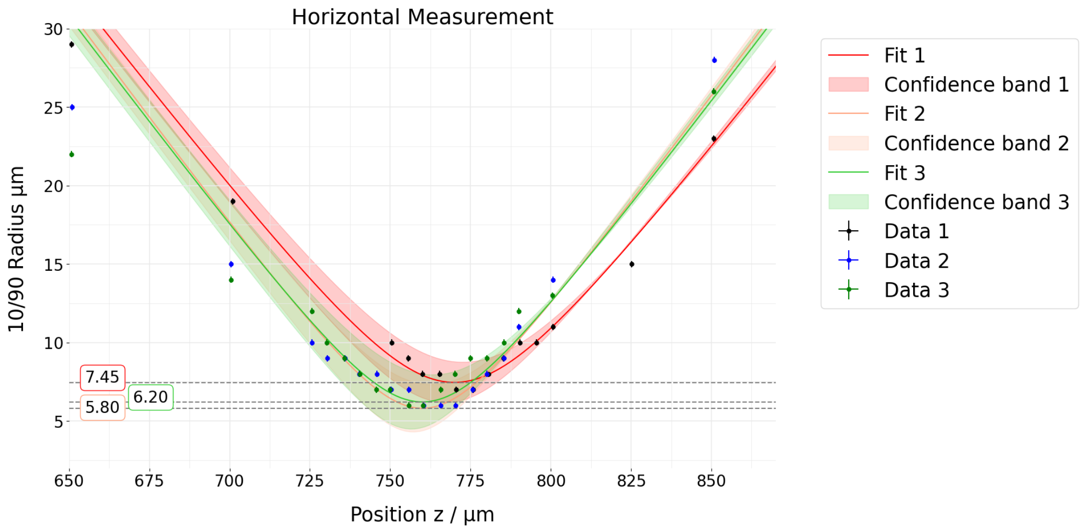

)

Fig. 4.6: Zoomed in plot of the 10/90 radius as a function of the position z of the knife edge for the incident beam $\lambda = 1064$nm. Eq 3.5 was used to fit the data. The resulting radii of the focal spot are; $r_1 = 7.45 \pm 1.28$ μm, $r_2 = 5.80 \pm 1.51$ μm, $r_3 = 6.20 \pm 1.72$ μm.

Upon examining the plot 4.5 along with the zoomed plot 4.6, it can be inferred that the focal spot in the horizontal direction is highly stable. The three measurements were fitted, and the resulting shift parameters were obtained as $z_{0_1} = 770.00 \pm 2.60$ μm, $z_{0_2} = 760.00 \pm 2.81$ μm, and $z_{0_3} = 760.00 \pm 3.39$ μm, which confirms the stability of the focal spot. Additionally, the 10/90 knife edge measurement provides an approximation of the radius of the beam, which is accurate within a certain degree of uncertainty. Therefore, averaging the r values, yields the average radius of the horizontal measurement as $r_{avg} = 6.48 \pm 1.50$ μm.

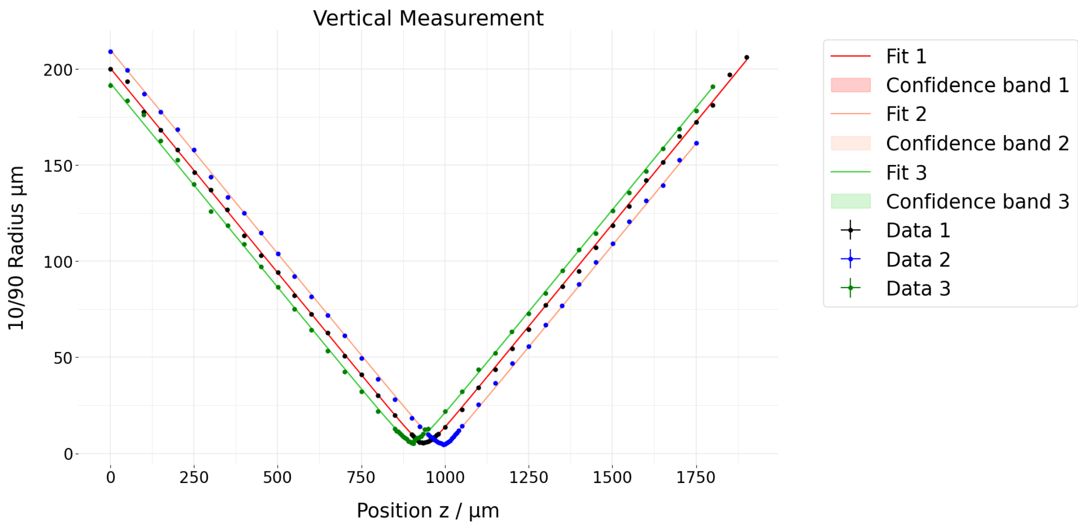

)

Fig. 4.7: Plot of the 10/90 radius as a function of the position z of the knife edge for the incident beam $\lambda = 1064$nm. Eq 3.5 was used to fit the data. The resulting radii at focal spot are; $r_1 = 5.33 \pm 0.39$ μm, $r_2 = 4.92 \pm 0.33$ μm, $r_3 = 6.49 \pm 0.37$ μm.

In the case of the vertical measurement, the plot 4.7 and its zoomed plot 4.8 confirm that the variations obtained from the vertical beam size measurement of the previous section are directly affecting the stability of the focal spot in the vertical direction. The resulting shift parameters obtained from fitting the three measurements are; $z_{0_1} = 937.10 \pm 0.55$ μm, $z_{0_2} = 992.33 \pm 0.47$ μm, and $z_{0_3} = 900.59 \pm 0.93$ μm. However, based on these measurements alone, it is not possible to determine if the beam exhibits any symmetric movement or if it stabilizes after a certain period. Nevertheless, the average radius of the three measurements is $r_{avg} = 5.58 \pm 0.36$ μm, regardless of the shift in each measurement.

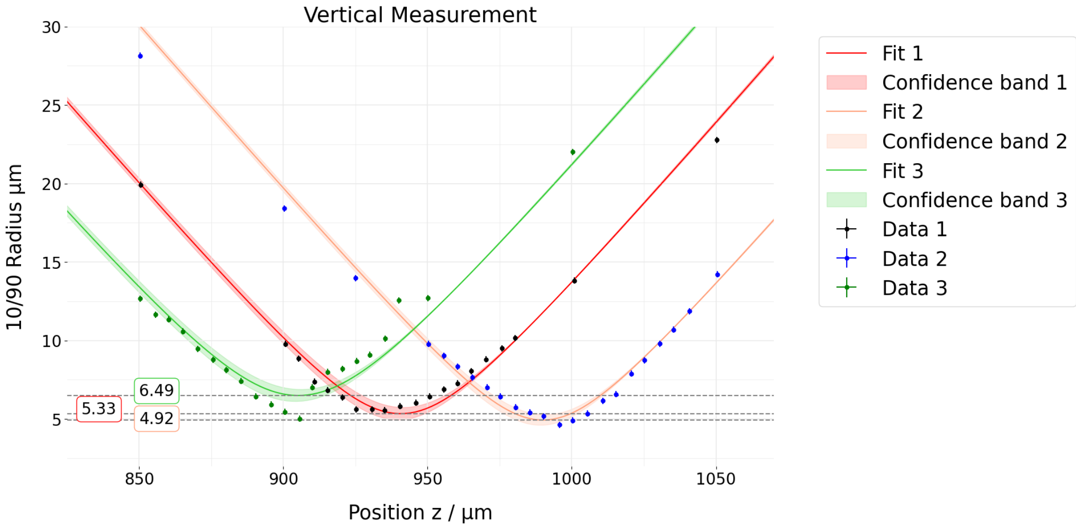

Fig. 4.8: Zoomed plot of the 10/90 radius as a function of the position z of the knife edge for the incident beam $\lambda = 1064$nm. Eq 3.5 was used to fit the data. The resulting radii at focal spot are; $r_1 = 5.33 \pm 0.39$ μm, $r_2 = 4.92 \pm 0.33$ μm, $r_3 = 6.49 \pm 0.37$ μm.

4.4. Focal spot size measurement

As previously mentioned, the size of the focal spot is crucial in determining the efficiency of the objective. Therefore, it is considered one of its most critical properties. A smaller focal spot leads to higher trap depth and better confinement of the atoms, resulting in a higher density of trapped atoms. Meaning that the atoms are tightly confined to the center of the trap, reducing the chances of them escaping due to thermal fluctuations or collisions with other atoms. Moreover, the loading rate of atoms into the trap is also affected by the size of the focal spot. A smaller focal spot leads to a higher loading rate as the atoms are more efficiently captured by the trap. Thus, accurate measurements of the focal spot size are essential to optimize the performance of the objective.

This section presents detailed knife edge measurements performed at various positions in the z direction for both the horizontal and vertical direction. The 2σ values acquired from each error function fit at different positions are plotted as a function of their corresponding position in z. Subsequently, the data is fitted using equation 3.5, which yields four key parameters, namely, the waist w_0, the offset z_0, the Rayleigh range z_R, and the quality beam factor M^2. These parameters are discussed in greater detail in section 3.3 and visually presented in Figure 2.5. Another important value computed is R^2, which reflects the quality of the fit. An R^2 value of 1 indicates the best fit possible.

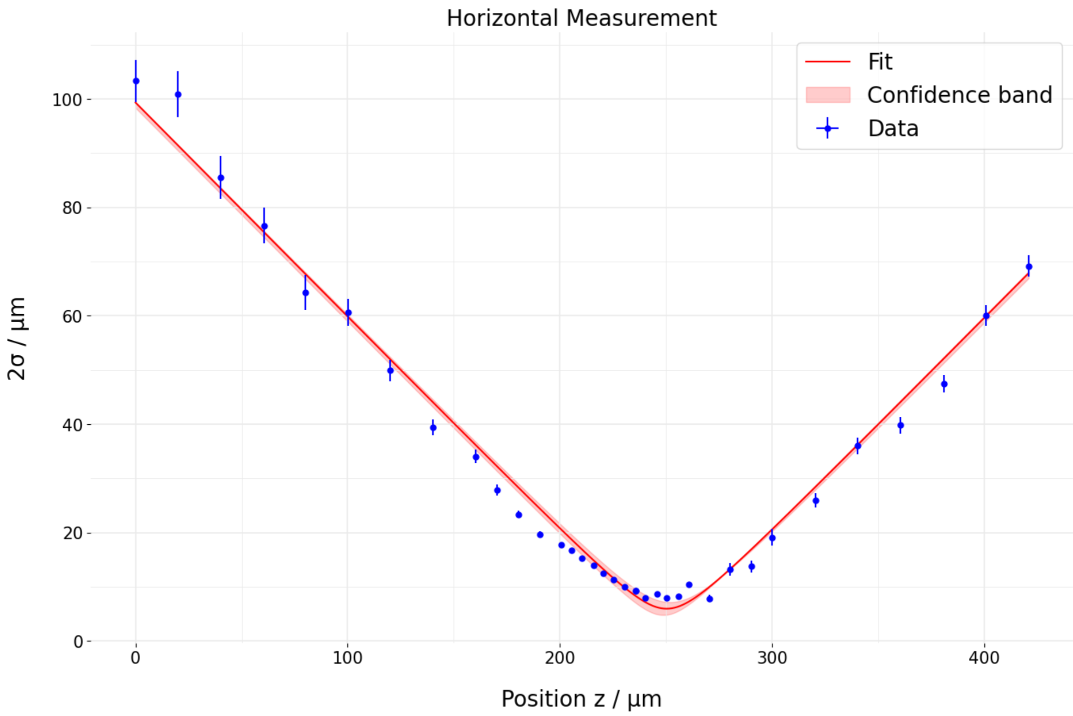

Fig. 4.9: Graph of the radii 2σ as a function of the position z of the knife edge for the incident beam $\lambda = 1064$nm. The data points are shown in blue and the fit function in red. The resulting fit parameters are; $w_0 = 5.94 \pm 1.18\mu m$, $z_0 = 250.28 \pm 1.58\mu m$, $z_R = 15.00 \pm 3.03\mu m$, $R^2 = 0.98$, with set $M^2 = 1$.

Upon analyzing the plot shown in Figure 4.9, it is apparent that there are noticeable fluctuations in the data points. As a result, the fitting of the data points with the Gaussian beam fit function 3.5 becomes uncertain. However, after trying various values of M^2, it was found that only $M^2 = 1$ provided the best fit for the data. It is important to note that the measurement for this plot took an entire day, and the AOM was turned on throughout the duration of the measurement.

Having the AOM turned on for an extended period can cause various negative effects on the beam quality. One of the most significant effects is the generation of acoustic noise that can cause fluctuations in the intensity of the laser beam. As a result, variations in the focal point size can occur, reducing the overall quality of the beam. In addition, it is known, that the AOM can generate heat. This, can cause thermal fluctuations that affect the beam quality. And since the longer the AOM is on, the warmer it gets, this is the most probable source of error. Thus, these fluctuations can cause beam drift and increased noise in the measurement, leading to inaccurate results.

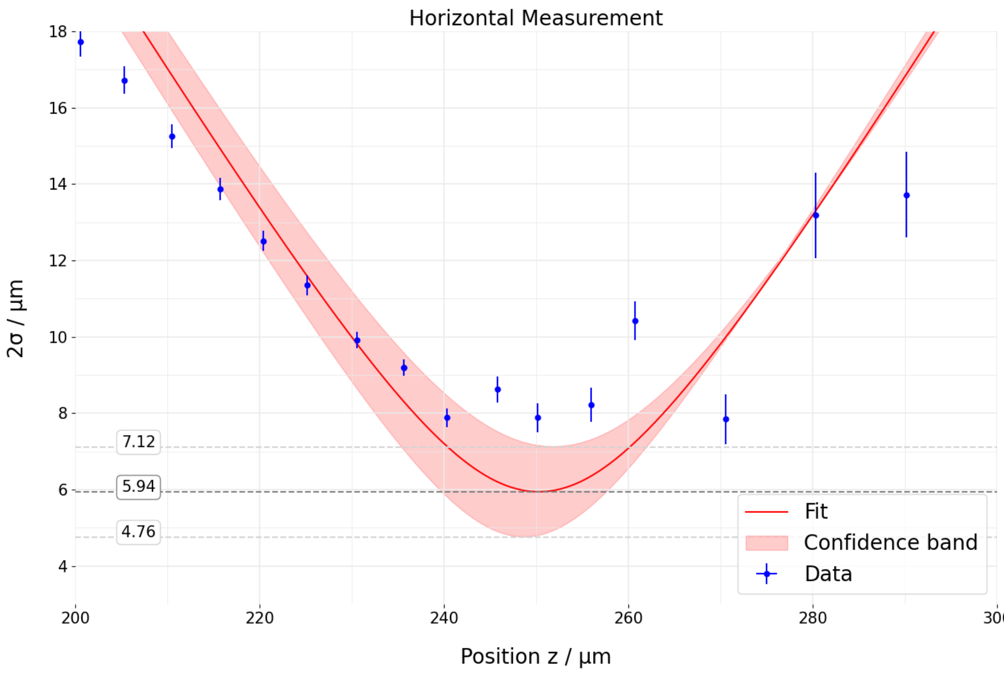

Fig. 4.10: Magnified graph of the radii 2σ as a function of the position z of the knife edge for the incident beam $\lambda = 1064$nm at focus. The data points are shown in blue and the fit function in red. The resulting fit parameters are; $w_0 = 5.94 \pm 1.18 \mu m$, $z_0 = 250.28 \pm 1.58 \mu m$, $z_R = 15.00 \pm 3.03 \mu m$, $R^2 = 0.98$, with set $M^2 = 1$.

To analyze the data points at the focal spot, a zoomed image of the previous plot 4.9 is presented in Figure 4.10. This enables a closer inspection, revealing that the fit does not match the data points in this range, possibly due to the influence of the overall data points of the measurement. Notably, significant fluctuations can be observed immediately after the focal point. The AOM is one source of error that can cause these fluctuations, but it is also possible that the knife edge may contribute to the observed deviations from the fit. This is because any imperfections on the knife edge or any misalignment of the knife edge with respect to the beam can cause distortions in the measured intensity distribution. These distortions can lead to inaccuracies in the beam profile measurements and affect the fitting of the data with the Gaussian beam fit function. It is uncertain whether the damage threshold of the knife edge measurement exceeds the power density $P_d = 1.77 \times 10^5 \mathrm{W/cm}^2$ for the focal point with a beam waist of $w_0 = 5.94 \pm 1.18 \mu$m and an average maximal power of $P = 200$mW.

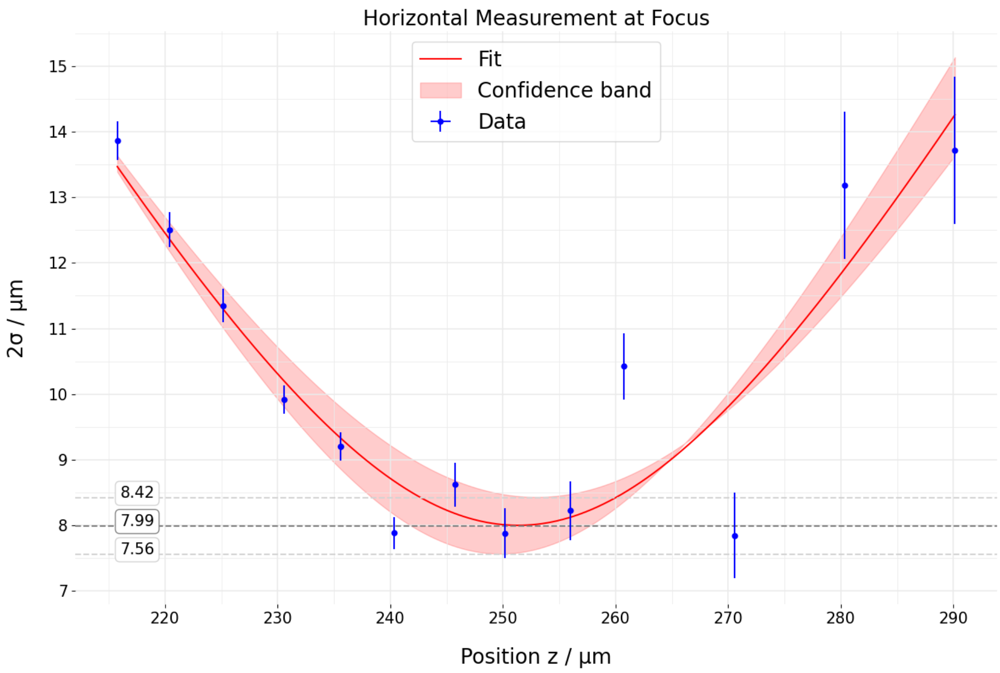

Fig. 4.11: Graph of the radii 2σ as a function of the position z of the knife edge for the incident beam $\lambda = 1064$nm at focus. These are cut data points from the overall measurement and are shown in blue and the fit function in red. The resulting fit parameters are; $w_0 = 7.99 \pm 0.43\mu m$, $z_0 = 251.36 \pm 1.58\mu m$, $z_R = 26.28 \pm 2.97\mu m$, $R^2 = 0.83$, with set $M^2 = 1$.

For the purpose of comparison, data points from the focal spot region were separated or better said isolated from the overall measured data points shown in Figure 4.9 and plotted with the exact same way, as shown in Figure 4.11. By doing so, a new fit could be performed on the isolated data points, resulting in parameters that are a better match to the data. The plot still shows noticeable fluctuations, particularly after the focal point. Although the lowest data points do not fit well with the Gaussian fit, they fall within the error range of the beam waist measurement, which is $w_0 = 7.99 \pm 0.43\mu m$. . It is worth noting that the focal point waist in this plot is significantly higher compared to the focal point waist $w_0 = 5.94 \pm 1.18\mu m$ obtained from the overall data points in Figure 4.10. To address this uncertainty, repeating the same measurement at least two more times and determining the average waist of all the measurements may be necessary.

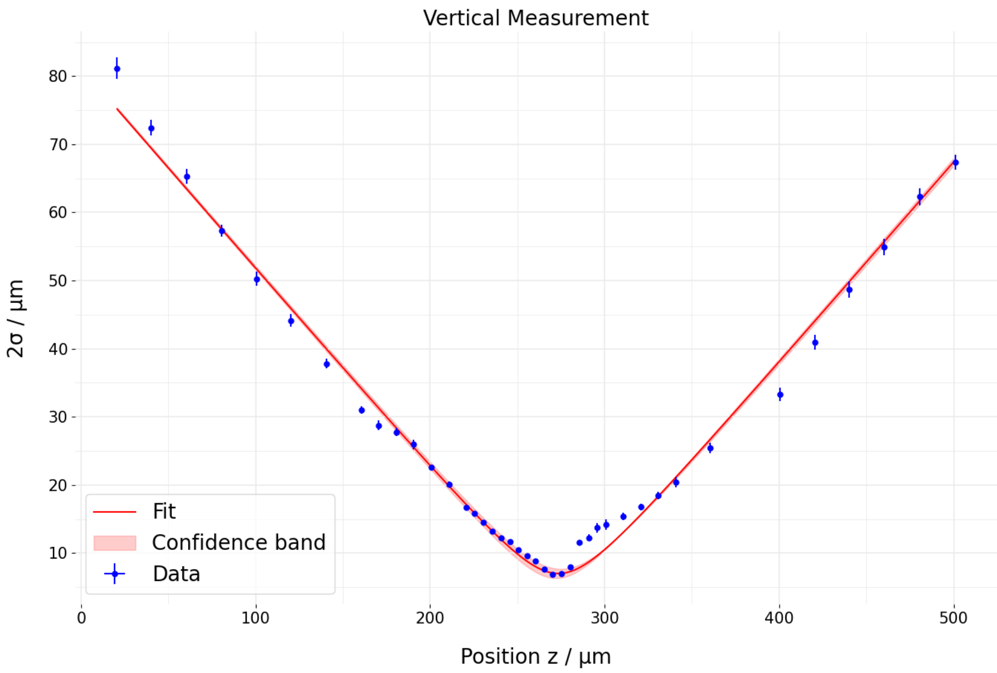

Fig. 4.12: Graph of the radii 2σ as a function of the position z of the knife edge for the incident beam $\lambda = 1064$nm. The data points are shown in blue and the fit function in red. The resulting fit parameters are; $w_0 = 6.99 \pm 0.67\mu m$, $z_0 = 273.53 \pm 1.37\mu m$, $z_R = 23.65 \pm 1.37\mu m$, $R^2 = 0.98$, with set $M^2 = 1$.

After examining the data of the vertical measurement, as displayed in Figure 4.12, notable fluctuations are observed directly following the focal spot. These fluctuations are similar to the data obtained from the third vertical knife edge measurement illustrated in Figure 4.8. Such similarities suggest that either the AOM is inducing a systematic effect on the beam, that can can only be detected on the vertical direction, or the knife edge was damaged during the focal point measurement, unable to withstand the high power density at that location.

Despite the fluctuations observed in the vertical measurement, the Gaussian function was found to be a better fit for the data points in comparison to the horizontal measurement. This was further confirmed by the zoomed version, which showed a good match between the fit and data points. For the purpose of analysis, data points from the focal point region were also isolated, similarly to Figure 4.11, from the overall measured data points and plotted with the exact same way. The resulting plot as well as the parameters were found to be in good agreement with the magnified version. Therefore, the initial parameters found in Figure 4.12 will be used for evaluation.

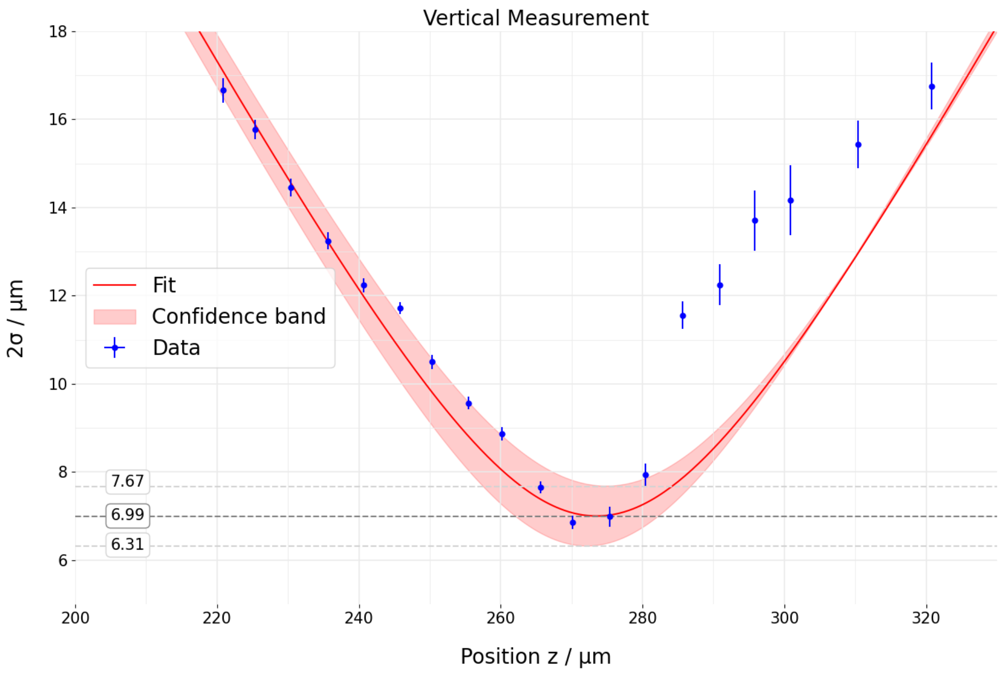

Fig. 4.13: Magnified graph of the radii 2σ as a function of the position z of the knife edge for the incident beam $\lambda = 1064$nm at focus. The data points are shown in blue and the fit function in red. The resulting fit parameters are; $w_0 = 6.99 \pm 0.67 \mu m$, $z_0 = 273.53 \pm 1.37 \mu m$, $z_R = 23.65 \pm 1.37 \mu m$, $R^2 = 0.98$, with set $M^2 = 1$.

To summarize the obtained focal spot waist values, the following Table 4.2 was created. The table includes theoretical expected values w_{Theo} obtained from the Zemax software, experimental values w_0 obtained from fitting the overall data points, and values $w_{0_{cut}}$ obtained from fitting the isolated focal point data points. Upon comparing the data, it can be inferred that the values of $w_{0_{cut}}$ are more reliable than the values of w_0. This is due to the beam's ellipticity, proven in section 4.2, where the size of the beam in the horizontal direction is larger compared to the vertical direction. Hence, a larger focal spot on the horizontal axis was anticipated.

Tab. 4.2: Focal point waist of Mk. II for $\lambda = 1064$nm.

	Horizontal	Vertical
w_{Theo} [μm]	1.50 ± 0.00	1.50 ± 0.00
w_0 [μm]	5.94 ± 1.18	6.99 ± 0.67
$w_{0_{cut}}$ [μm]	7.99 ± 0.43	6.99 ± 0.67

4.5. Resolution measurement

As stated in section 3.5, measuring the resolution of a objective is crucial because it provides an estimation of the accuracy with which atoms can be positioned and manipulated, as well as how closely they can be trapped. To ensure accurate imaging, an achromatic doublet lens was attached to the objective ($f = 1000$ mm), reducing the effects of chromatic aberration. The beam size was also decreased by coupling the beam into a fiber rather than using magnification stages, which was done in the previous experimental setup shown in Figure 4.1. A schematic of the experimental setup for measuring resolution is shown in Figure 3.7.

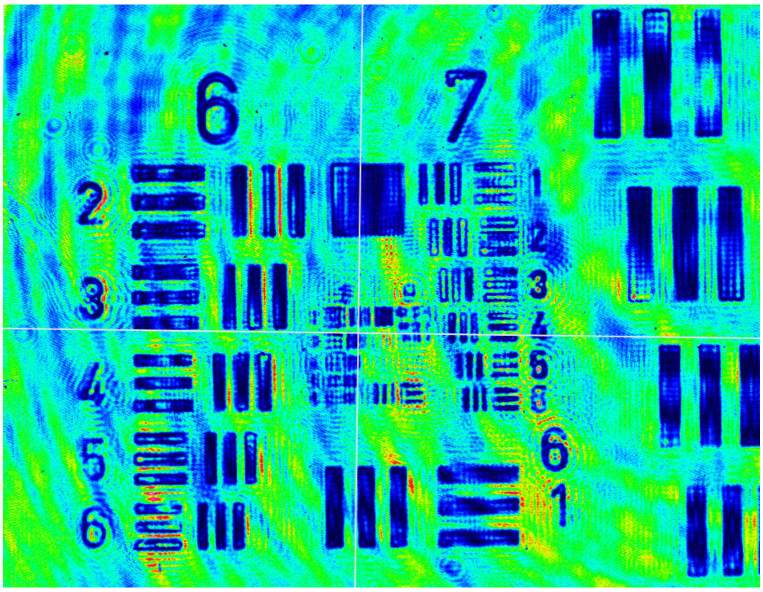

Fig. 4.14: Imaging the USAF 1951 resolution chart.

To achieve high-resolution imaging, precise alignment within the range of micrometers is required. This means that investing more time in setup alignment with utmost precision can probably lead to better imaging than the current one. The current optimal resolution imaging is presented in Figure 4.14. It is worth noting that the target used is a negative USAF 1951 target, where chrome covers the substrates, leaving the patterns clear and resulting in high reflectivity. The image was taken with a beam profiler camera [3], with pixel size of 5.5×5.5 μm. The aim of the alignment is to be able to observe a line pairs at the highest group with the highest element possible. Once this is achieved, the corresponding group and element numbers can be plugged into eq 3.7. The number of lines per millimeter for the groups and elements shown in Figure 4.14 are tabulated in Table 4.3.

[3] Edmund Optics Beam Profiler 4M

Tab. 4.3: Number of line pairs per millimeter in the USAF 1951 resolution test target.

	Group number			
Element	6	7	8	9
1	64.0	128.0	256.0	512.0
2	71.8	143.7	287.4	574.7
3	80.6	161.3	322.5	645.1
4	90.5	181.0	362.0	724.1
5	101.6	203.2	406.4	812.7
6	114.0	228.1	456.1	912.3

Since the aim of this measurement is to be able to observe a line pairs at the highest group with the highest element possible. Zooming into the resolution image at Group 8 Element 1, one can distinguish the line pairs on the chart, as shown in Figure 4.15. Therefore, this level of resolution will be considered as the highest resolution achieved by the microtrap objective.

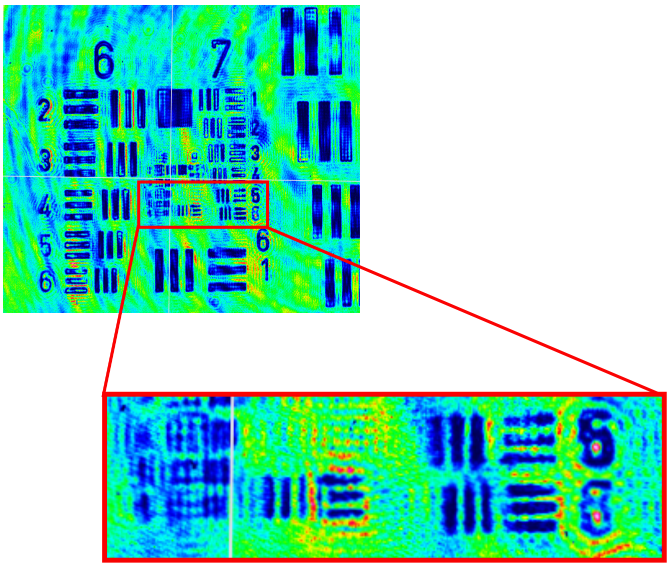

Fig. 4.15: Image of the resolution using the USAF 1951 target. Maximum resolution achieved is Group 8 Element 1.

For a better understanding of the resolution value, one can refer to the table below A.2 which shows the width values of each line in their corresponding group and element number.

Tab. 4.4: Width of a line in micrometers in the USAF 1951 resolution test target.

	Group number			
Element	6	7	8	9
1	7.81	3.91	1.95	0.98
2	6.96	3.48	1.74	0.87
3	6.20	3.10	1.55	0.87
4	5.52	2.76	1.38	0.69
5	4.92	2.46	1.23	0.62
6	4.38	2.19	1.10	0.55

In conclusion, the objective can resolve an image of a line with a width of $w = 1.95$ μm. Therefore, the magnification of the imaging system can be inferred as -31.4, which matches well with the focal length of 31.85 mm.

5. Outlook & Discussion

In this work, we were able to characterize a high numerical aperture objective. We introduced the concept of optical aberrations and their impact on the performance of the objective. Additionally, we discussed how the size and profile of the laser beam directly impacts its performance. To test this, we used knife-edge measurements to estimate the size of the incident beam and obtained the values $4\sigma = 28.90 \pm 0.18$ μm in the horizontal and $4\sigma = 20.46 \pm 0.17$ μm in the vertical direction, respectively, indicating that the beam is clearly elliptic. However, as stated previously, the objective was designed to work with gaussian beams and performance is negatively impacted when using elliptic beams. To investigate this and to determine the stability of the focus over extended operation, we used the 10-90 knife-edge method to estimate the size of the beam close to the focal region. It was evident that the beam also behaves elliptically in the focal region and that there is a statistical variation in the measured values of beam size over multiple attempts. These deviations may have been caused by either a non-optimal coupling of the beam into the AOM or because the laser is unstable in the vertical direction. Next, more detailed and precise measurements of the focal spot waist in both horizontal and vertical direction were performed using a knife-edge mounted on a high precision piezoelectric translation stage. This resulted in the values of $w_0 = 7.99 \pm 0.43$ μm in the horizontal direction and $w_0 = 6.99 \pm 0.67$ μm in the vertical direction. The data obtained from these measurements displayed noticable variations over multiple runs, especialy right after the focal spot, which could have originated from several sources of error such as acoustic noise, thermal effects generated by the AOM, or imperfections and misalignment of the knife edge. Finally, the objective's resolution was estimated using a USAF 1951 chart, yielding an approximate spatial resolution of 2 μm. From this data, we can conclude that the objective should perform adequately and is ready for installation in the Dysprosium experiment. However, performance could be improved further if the incident beam was more Gaussian. This can be done by using beam shaping techniques to reduce ellipticity in the beam. Notably, cylindrical lenses are routinely employed to circularize elliptical beams. In the future, further tests can be carried out to characterize the performance of the objective more accurately. For e.g. one could measure the Field of View (FOV) of the objective, which is the region within which diffraction limited performance can be expected. On the other hand, a more precise technique to measure the diffraction limited resolution would be to measure the Point Spread Function (PSF), which describes the response of an optical system when imaging a point source of light. A more comprehensive description of an objective's performance usually includes these metrics. Furthermore, the techniques and concepts learned from this design and testing can be easily translated to design objectives for other experiments.

The design is inherently flexible and can be optimized for different wavelengths and/or different working distances. A separate imaging objective, optimized for operating at a wavelength of 626 nm has already been designed and is under assembly. Once assembled and installed, this imaging objective will be used to collect fluorescence from Dysprosium atoms trapped inside the ODT.

A. Appendix

A.1. Optical objective specifications

Tab. A.1: Objective consists of five stock elements from Thorlabs.

	S/N	Glass	EFL	D	R_1	R_2	CT
1	LC1093-C	N-BK7	-99.6	50.8	-51.5	0	4.00
2	LB1106-C	N-BK7	124.6	50.8	127.4	-127.4	8.1
3	LA1417-C	N-BK7	149.5	50.8	77.3	0	7.3
4	LE1418-C	N-BK7	149.5	50.8	47.9	119.3	5.10
5	LE1076-C	N-BK7	99.7	50.8	30.3	65.8	9.7

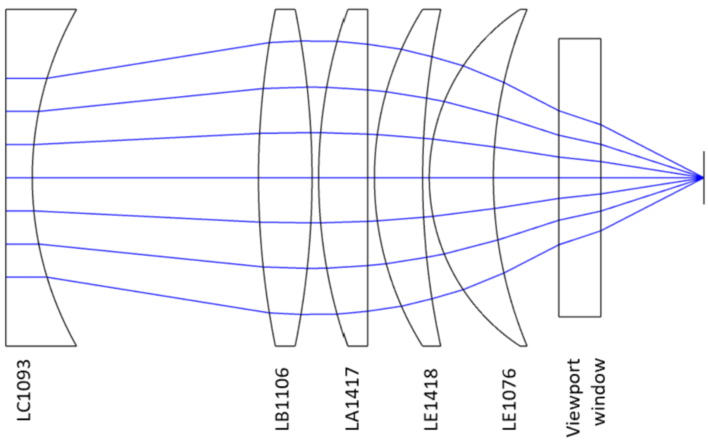

Fig. A.1: Lenses in the OpticStudio simulation.

Operating wavelength	1064 nm (trapping)
	626 nm (probing)
	421 nm (probing)
Back focal length (BFL)	> 31.85 mm
Maximum overall length (OAL)	< 150 mm
Numerical aperture (NA)	0.53
Strehl ratio (on axis)	> 0.8

Tab. A.2: Data of the lenses

Surface	**Name**	**Material**	**Radius**	**Thinkness**	**Full Aperture**
Obj.		Air	∞	$\boldsymbol{T_0}$	
1	LC1093	N-BK7	∞	4.00	34.07
2		Air	51.5	$\boldsymbol{T_2}$	33.93
3	LB1106	N-BK7	127.4	8.10	46.77
4		Air	-127.4	1.00	46.77
5	LA1417	N-BK7	77.3	7.30	46.68
6		Air	∞	1.00	46.38
7	LE1418	N-BK7	47.9	7.30	45.87
8		Air	119.3	1.00	45.04
9	LE1076	N-BK7	30.34	9.70	45.87
10		Air	65.8	$\boldsymbol{T_{10}}$	45.04
11	VIEWPORT	SILICA	∞	6.35	34.82
12		Vacuum	∞	15.60	34.21

Distances $\boldsymbol{T_0}$, $\boldsymbol{T_2}$ and $\boldsymbol{T_{10}}$ are on-axis distances between the surfaces:
$\boldsymbol{T_0}$: Distance from the source point to the negative element.
$\boldsymbol{T_2}$: Distance between the negative element to the positive triplet.
$\boldsymbol{T_{10}}$: Distance between the last element to the vacuum viewport window.

A.2. Plotting methods and error determination

The data was plotted and analysed using Python with the libraries NumPy, Matplotlib, and Scipy.

First, we read the data into NumPy arrays. Next, we use the SciPy library to obtain fitting errors. Specifically, we use the scipy.optimize.curve.fit function, which utilizes least squares to fit a user-defined function to the data while taking into account specified errors.

To calculate the error propagation of a variable $f(\vec{x})$ with known errors $\Delta x_1, \Delta x_2, ..., \Delta x_n$, we use the following formula:

$$\Delta f(\vec{x}) = \sqrt{\left(\frac{\partial f}{\partial x_1}\right)^2 + \left(\frac{\partial f}{\partial x_2}\right)^2 + ... + \left(\frac{\partial f}{\partial x_n}\right)^2}. \tag{A.1}$$

A.3. Assembly and experimental setup pictures

[a] 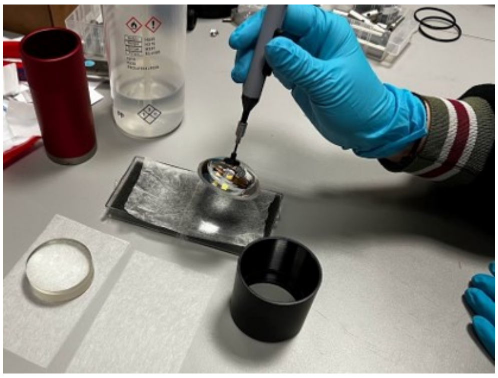 [b] 

Fig. A.2: [a] Process of objective assembly and [b] after assembly.

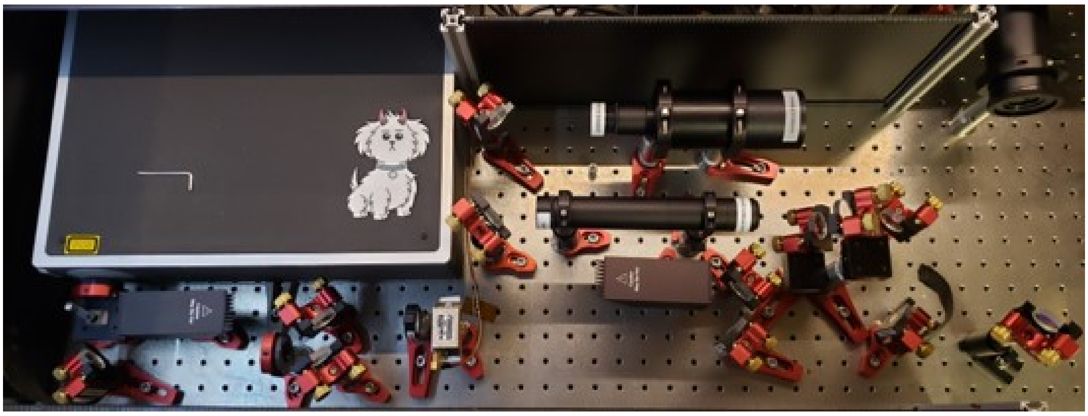

Fig. A.3: Experimental setup of the Mephisto MOPA 1064 nm laser and magnification stages.

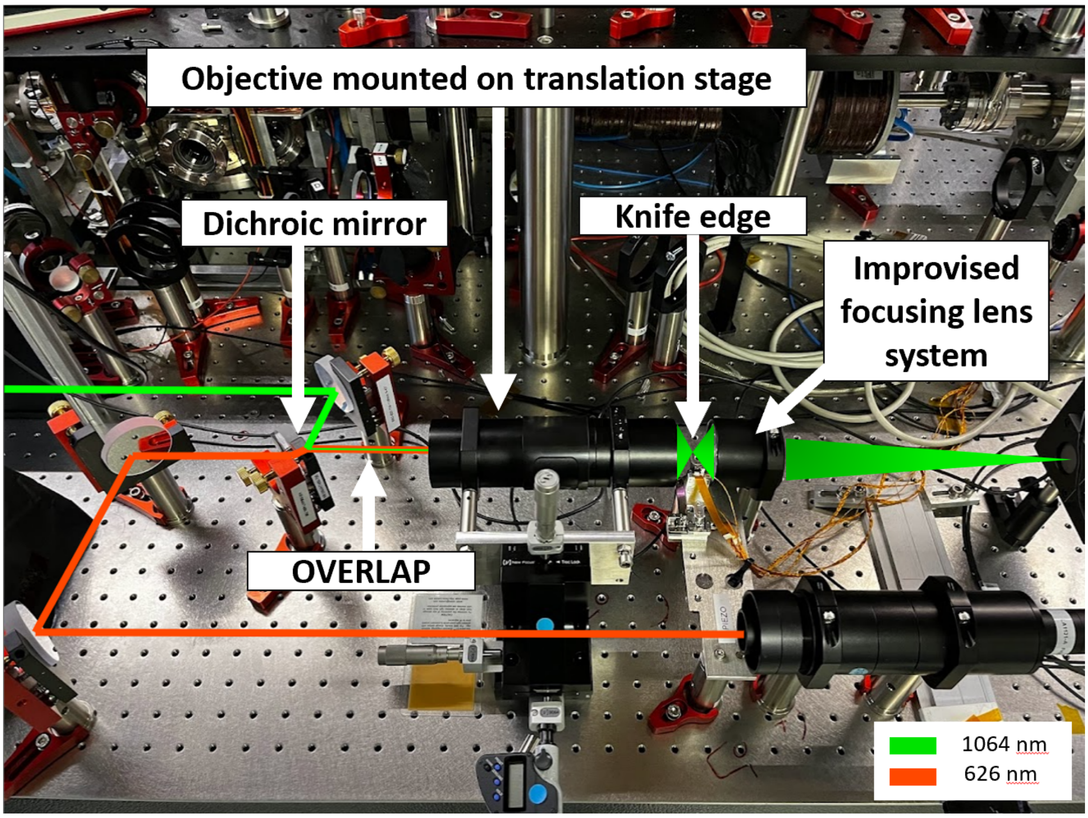

Fig. A.4: Experimental setup for the knife edge measurement with the piezoelement.

A.4. Tables for horizontal measurement

The obtained data from the detailed and precise measurement of the focal spot are presented in the following plots, where x is the position of the knife edge, r is the radius obtained from the 10-90 method and σ is the parameter obtained from the fit.

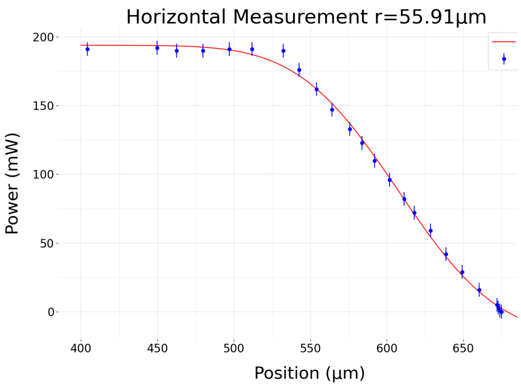

Fig. A.5: $x = 0\mu m$, $\sigma = 51.63 \pm 1.97\mu m$

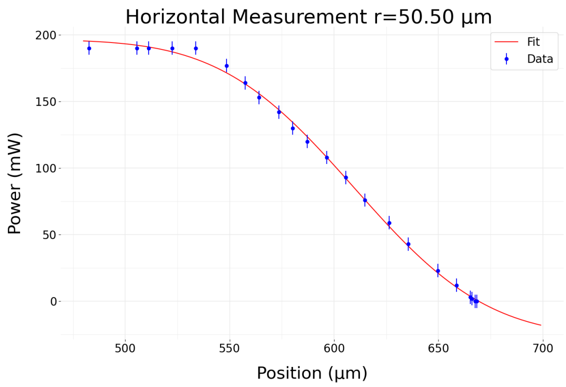

Fig. A.6: $x = 20.04\mu m$, $\sigma = 50.44 \pm 2.11\mu m$

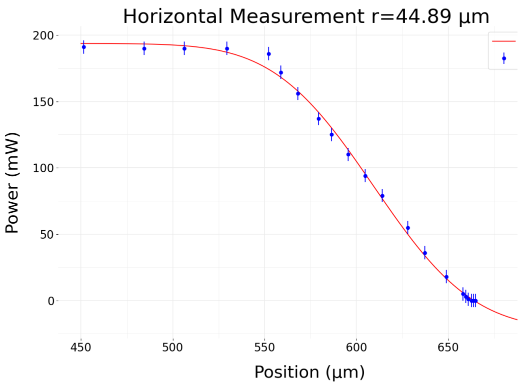

Fig. A.7: $x = 40.04\mu m$, $\sigma = 42.75 \pm 1.97\mu m$

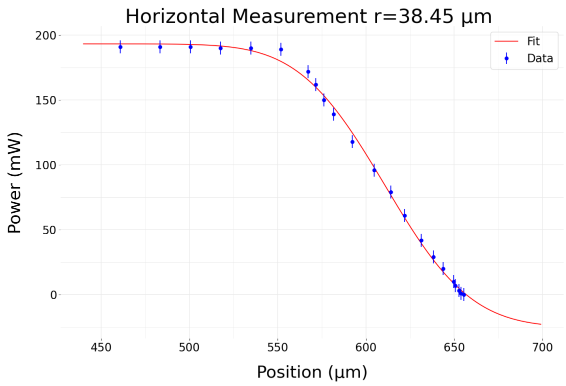

Fig. A.8: $x = 60.80\mu m$, $\sigma = 38.30 \pm 1.65\mu m$

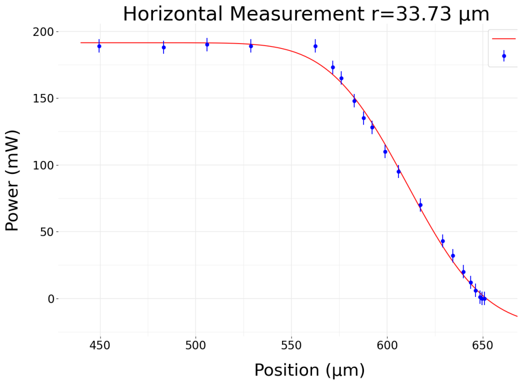

Fig. A.9: $x = 80.16.\mu m$, $\sigma = 32.13 \pm 1.61\mu m$

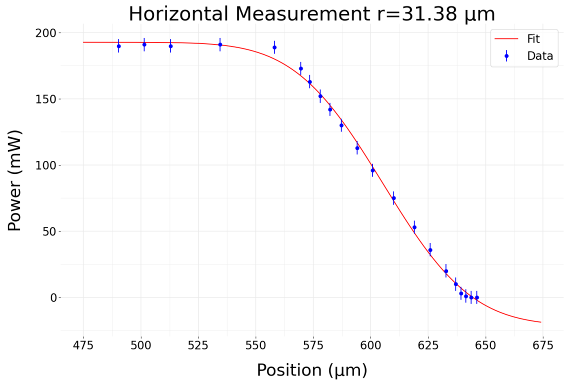

Fig. A.10: $x = 100.14\mu m$, $\sigma = 30.31 \pm 1.21\mu m$

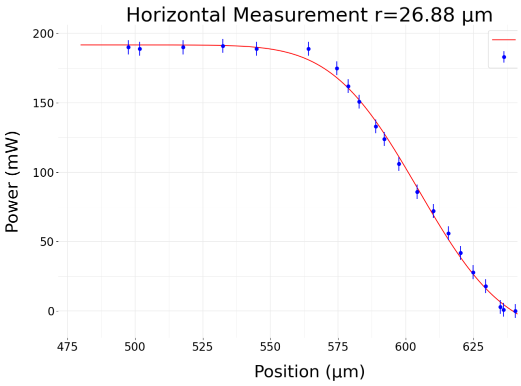

Fig. A.11: $x = 120.07\mu m$, $\sigma = 24.93 \pm 0.969\mu m$

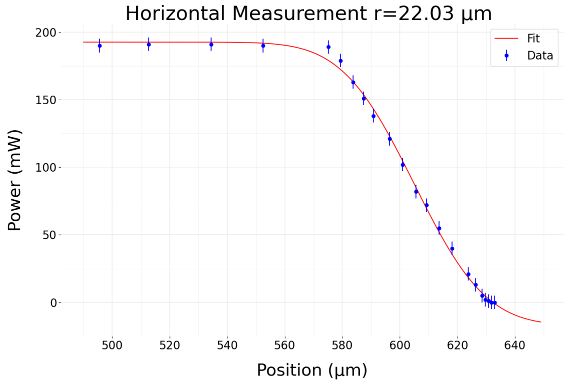

Fig. A.12: $x = 140.32\mu m$, $\sigma = 19.67 \pm 0.73\mu m$

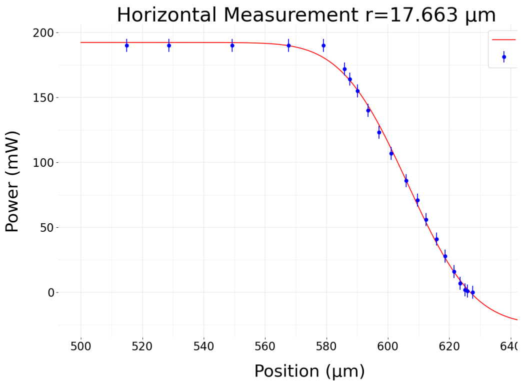

Fig. A.13: $x = 160.28\mu m$, $\sigma = 17.02 \pm 0.65\mu m$

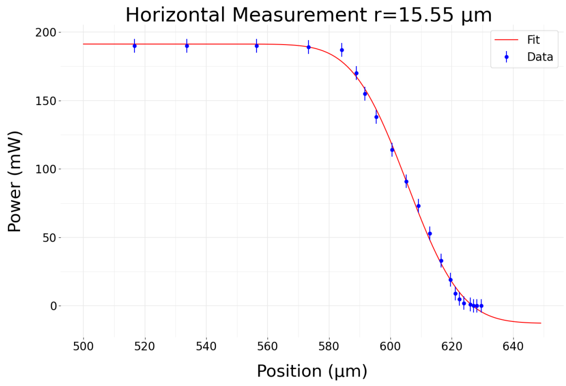

Fig. A.14: $x = 170.49\mu m$, $\sigma = 13.92 \pm 0.51\mu m$

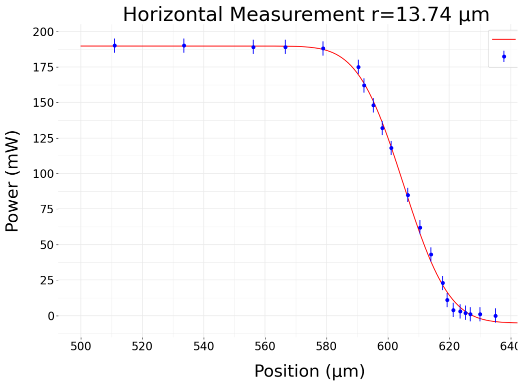

Fig. A.15: $x = 180.40\mu m$, $\sigma = 11.66 \pm 0.32\mu m$

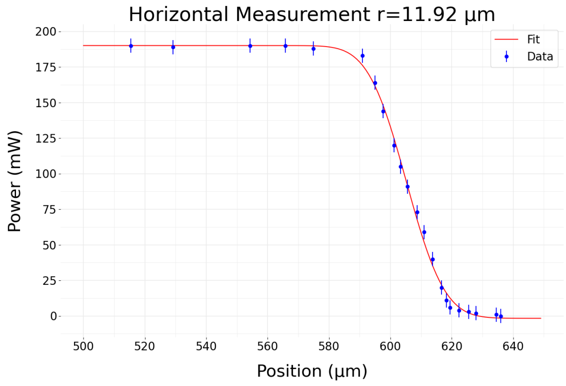

Fig. A.16: $x = 190.58\mu m$, $\sigma = 9.83 \pm 0.28\mu m$

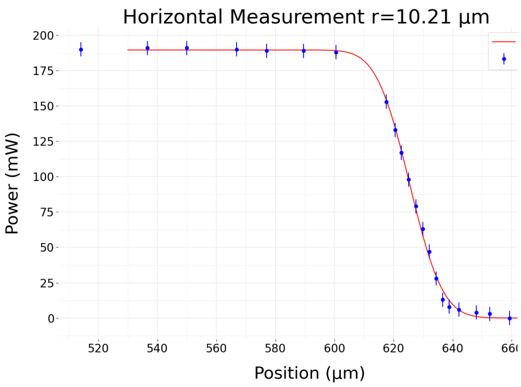

Fig. A.17: $x = 200.58\mu m$, $\sigma = 8.86 \pm 0.20\mu m$

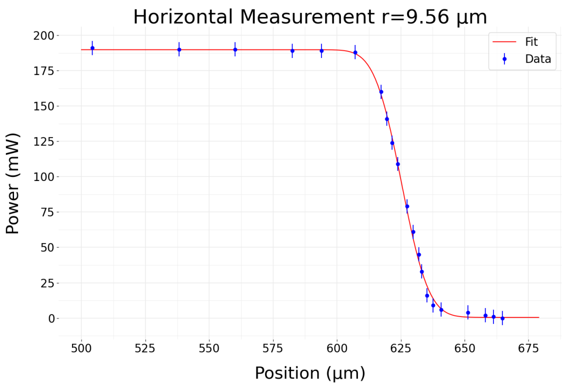

Fig. A.18: $x = 205.31\mu m$, $\sigma = 8.36 \pm 0.17\mu m$

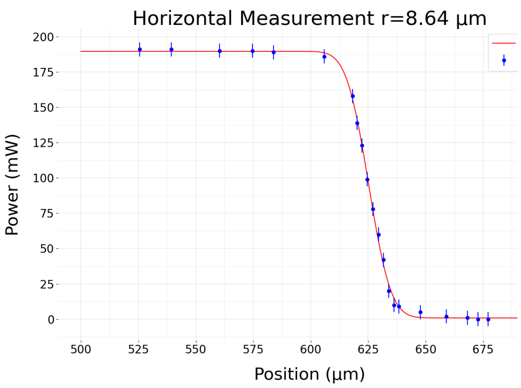

Fig. A.19: $x = 210.51\mu m$, $\sigma = 7.62 \pm 0.155\mu m$

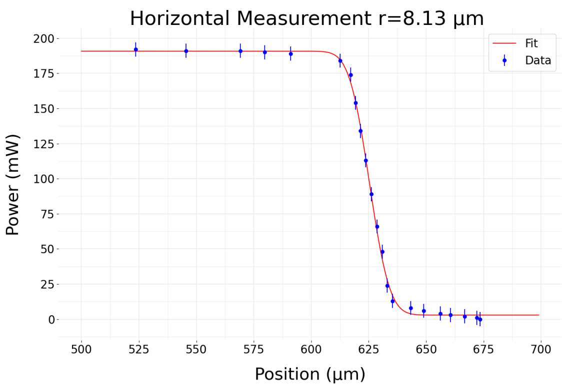

Fig. A.20: $x = 215.76\mu m$, $\sigma = 6.93 \pm 0.14\mu m$

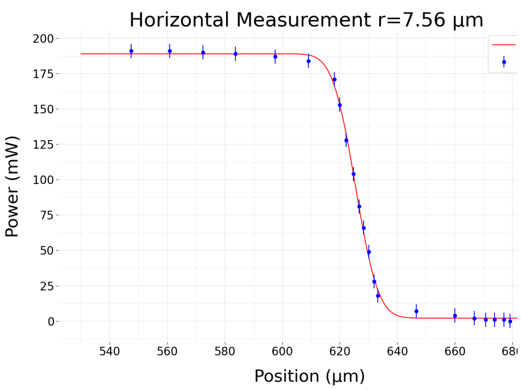

Fig. A.21: $x = 220.4\mu m$, $\sigma = 6.25 \pm 0.13\mu m$

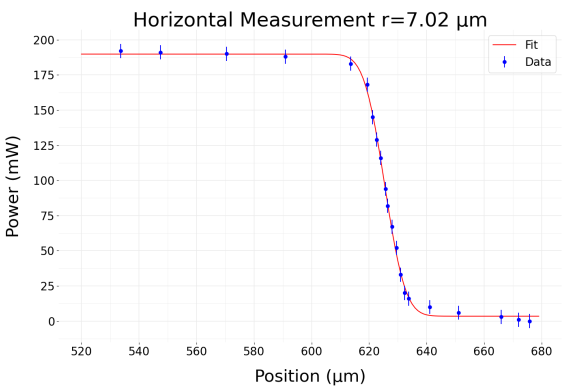

Fig. A.22: $x = 225.1\mu m$, $\sigma = 5.67 \pm 0.12\mu m$

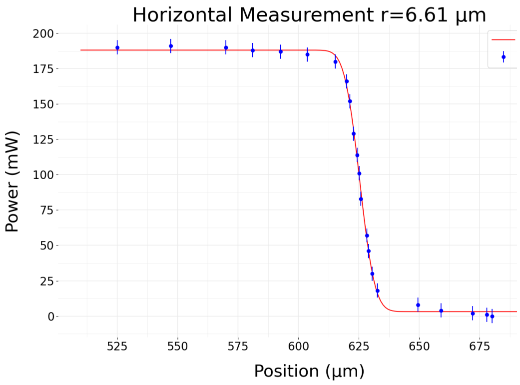

Fig. A.23: $x = 230.5\mu m$, $\sigma = 4.95 \pm 0.10\mu m$

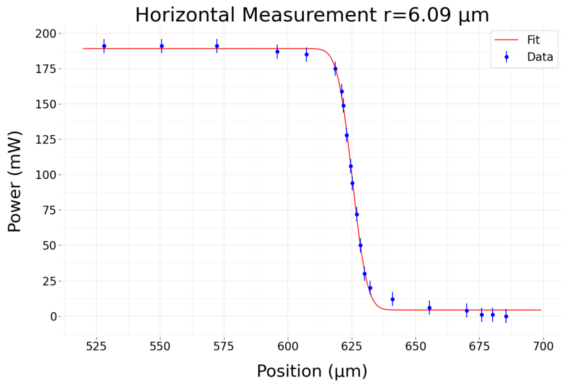

Fig. A.24: $x = 235.6\mu m$, $\sigma = 0.10 \pm 2.11\mu m$

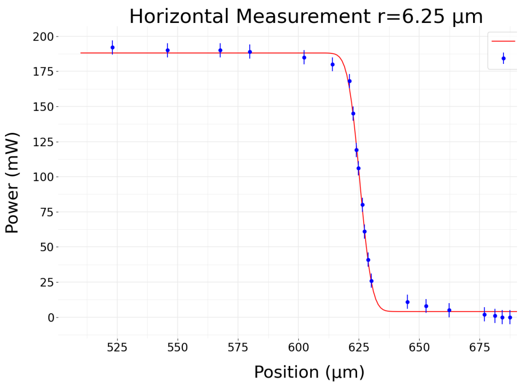

Fig. A.25: $x = 235.6\mu m$, $\sigma = 4.60 \pm 0.108\mu m$

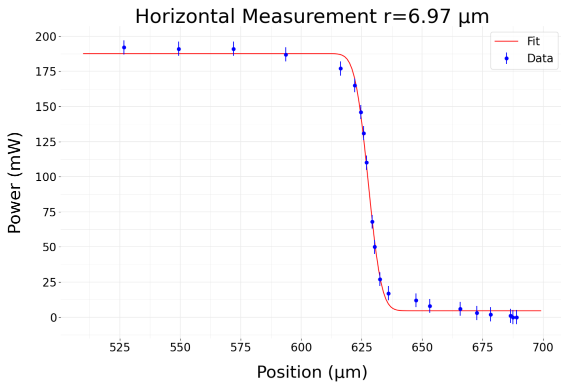

Fig. A.26: $x = 240.3\mu m$, $\sigma = 3.94 \pm 0.11\mu m$

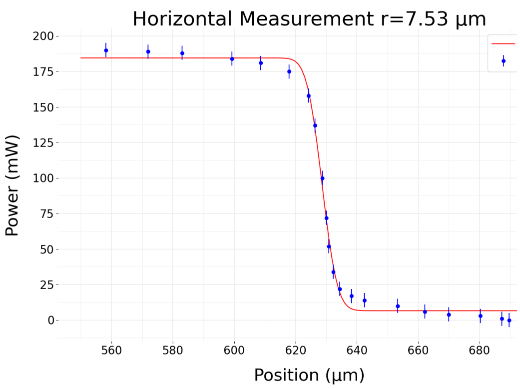

Fig. A.27: $x = 245.7\mu m$, $\sigma = 4.31 \pm 0.16\mu m$

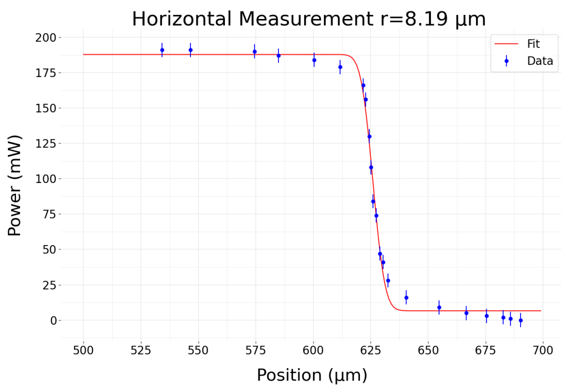

Fig. A.28: $x = 250.1\mu m$, $\sigma = 3.94 \pm 0.19\mu m$

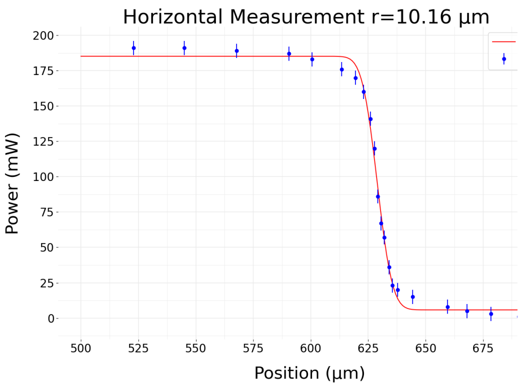

Fig. A.29: $x = 255.9\mu m$, $\sigma = 4.11 \pm 0.22\mu m$

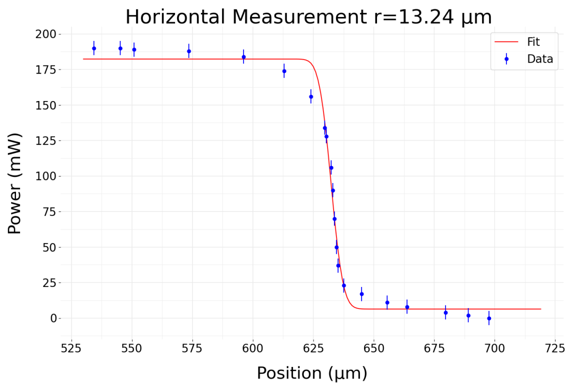

Fig. A.30: $x = 260.7\mu m$, $\sigma = 5.21 \pm 0.25\mu m$

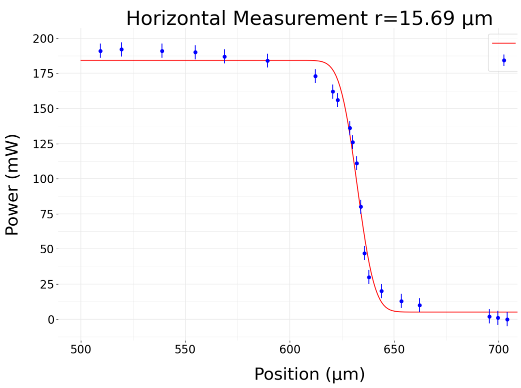

Fig. A.31: $x = 270.5\mu m$, $\sigma = 3.92 \pm 0.32\mu m$

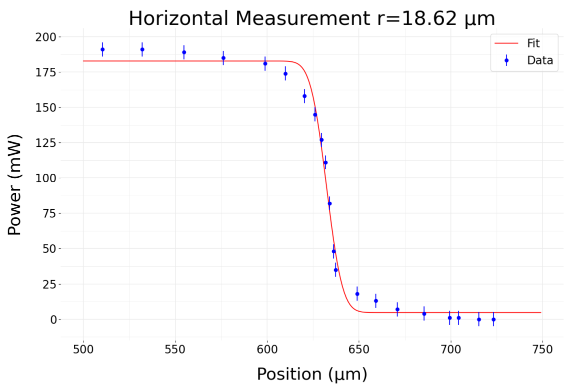

Fig. A.32: $x = 280.3\mu m$, $\sigma = 6.59 \pm 0.56\mu m$

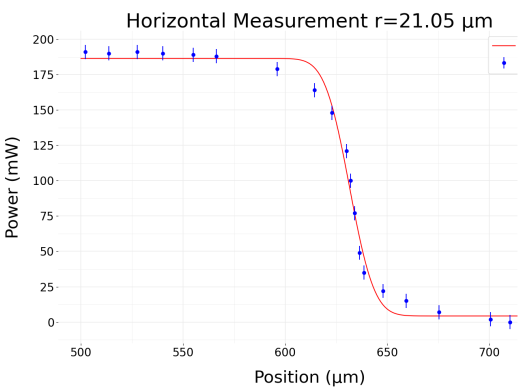

Fig. A.33: $x = 290.1\mu m$, $\sigma = 6.85 \pm 0.55\mu m$

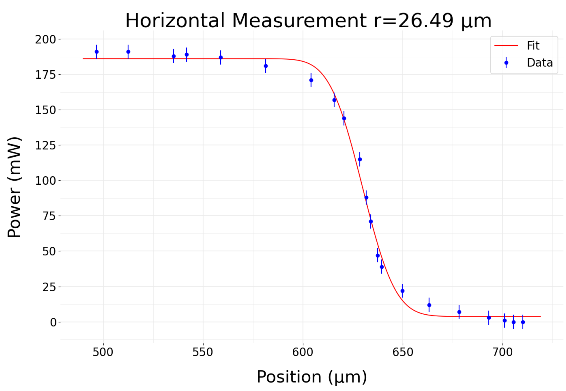

Fig. A.34: $x = 300\mu m$, $\sigma = 9.56 \pm 0.77\mu m$

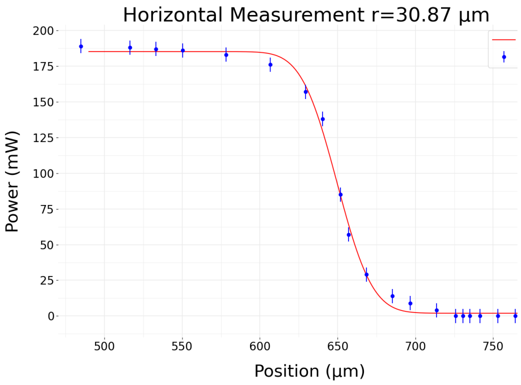

Fig. A.35: $x = 320.3\mu m$, $\sigma = 12.98 \pm 0.68\mu m$

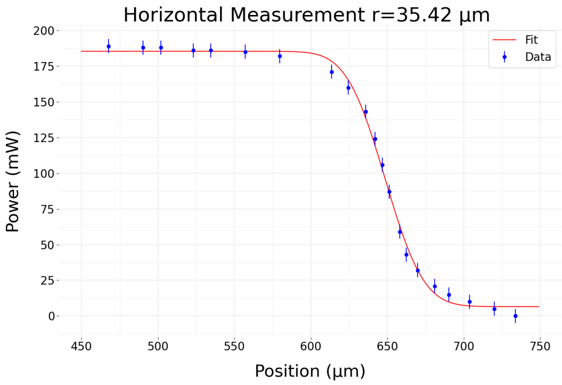

Fig. A.36: $x = 340.2\mu m$, $\sigma = 17.98 \pm 0.78\mu m$

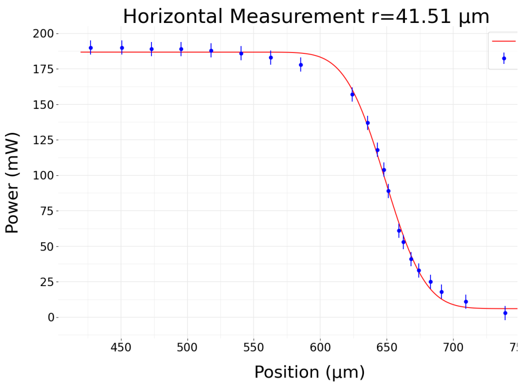

Fig. A.37: $x = 360.4\mu m$, $\sigma = 19.88 \pm 0.74\mu m$

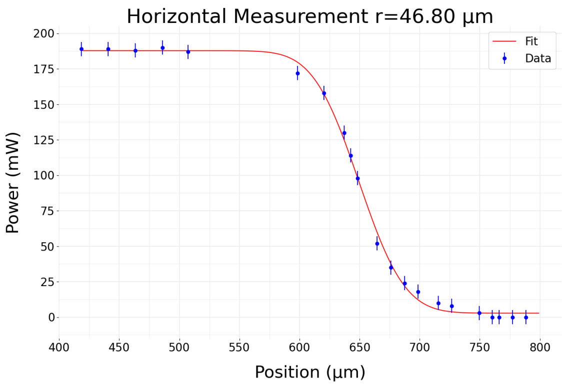

Fig. A.38: $x = 380.8\mu m$, $\sigma = 23.71 \pm 0.83\mu m$

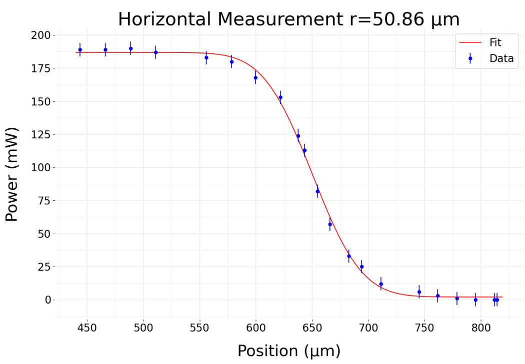

Fig. A.39: $x = 400.7\mu m$, $\sigma = 34.57 \pm 0.98\mu m$

A.5. Tables for vertical measurement

Same as in the case of the measurements for the horizontal direction. The obtained data from the detailed and precise measurement of the focal spot are presented in the following plots, where x is the position of the knife edge, r is the radius obtained from the 10-90 method and σ is the parameter obtained from the fit.

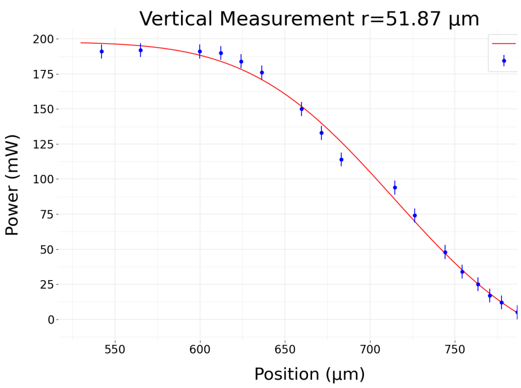

Fig. A.40: $x = 0\mu m$, $\sigma = 66.38 \pm 4.11\mu m$

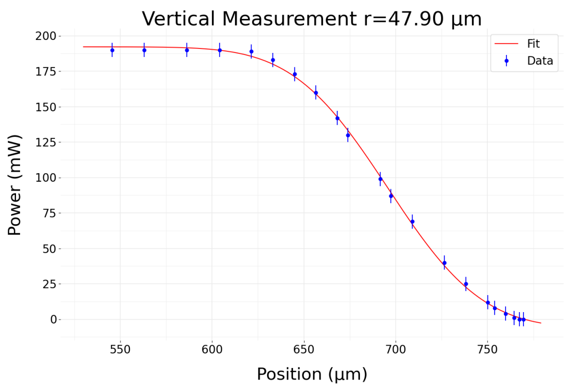

Fig. A.41: $x = 20.64\mu m$, $\sigma = 40.58 \pm 0.80\mu m$

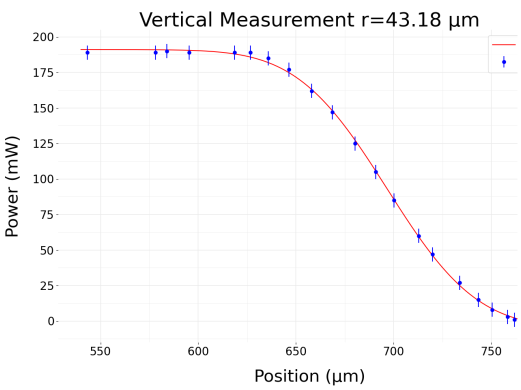

Fig. A.42: $x = 40.25\mu m$, $\sigma = 36.21 \pm 0.57\mu m$

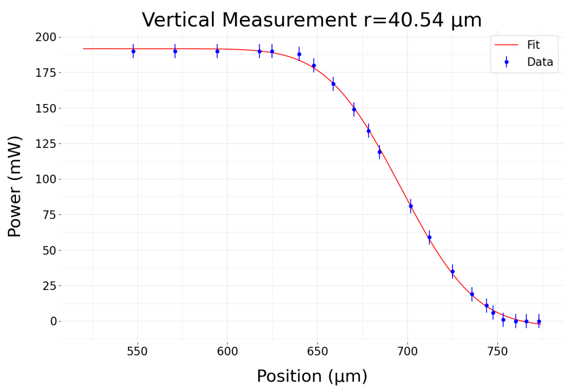

Fig. A.43: $x = 60.38\mu m$, $\sigma = 32.65 \pm 0.54\mu m$

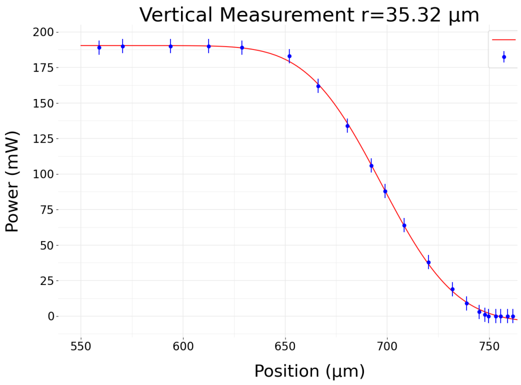

Fig. A.44: $x = 80.33\mu m$, $\sigma = 28.67 \pm 0.43\mu m$

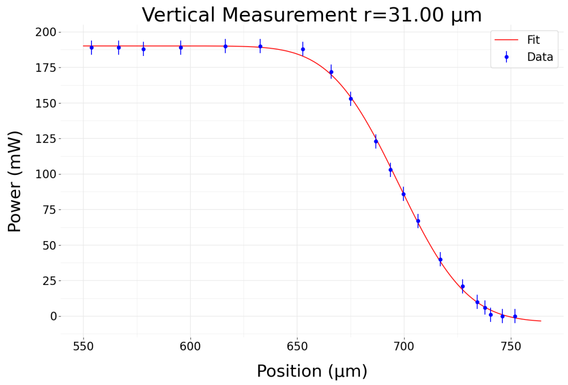

Fig. A.45: $x = 100.4\mu m$, $\sigma = 25.13 \pm 0.50\mu m$

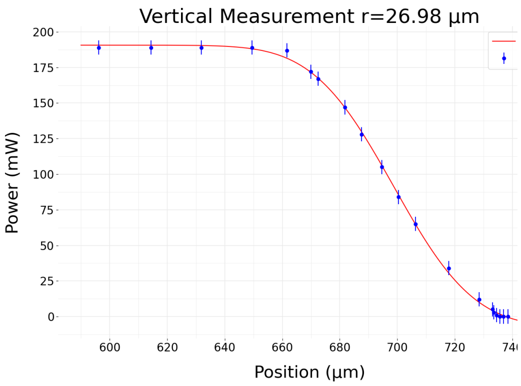

Fig. A.46: $x = 120.2\mu m$, $\sigma = 22.07 \pm 0.45\mu m$

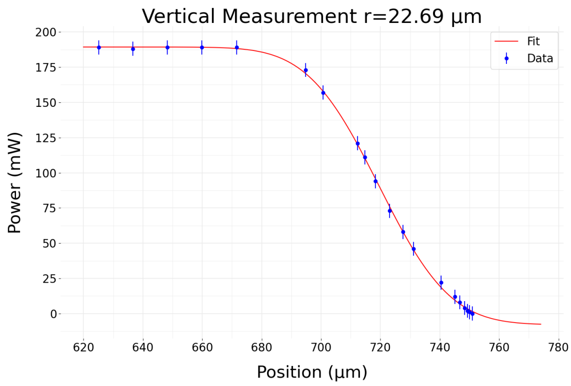

Fig. A.47: $x = 140.6\mu m$, $\sigma = 18.90 \pm 0.36\mu m$

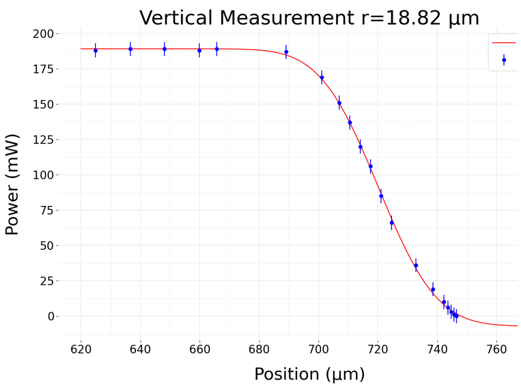

Fig. A.48: $x = 1605\mu m$, $\sigma = 15.50 \pm 0.28\mu m$

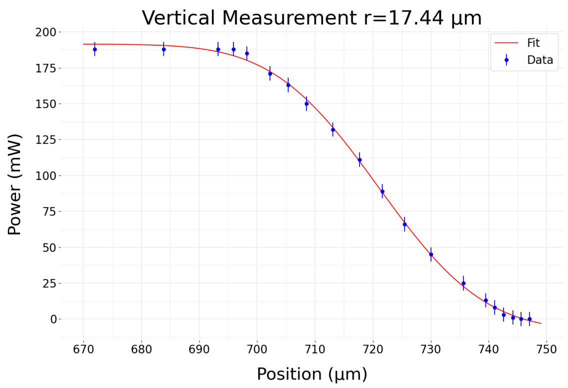

Fig. A.49: $x = 170.4\mu m$, $\sigma = 14.37 \pm 0.36\mu m$

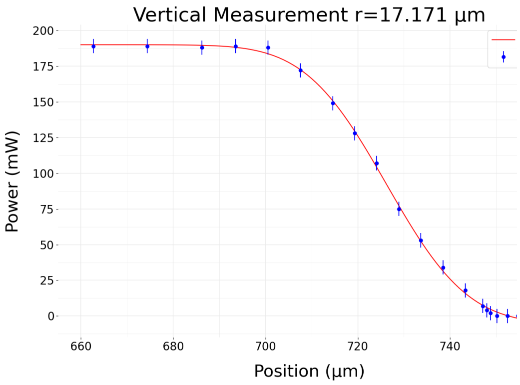

Fig. A.50: $x = 180.7\mu m$, $\sigma = 13.88 \pm 0.29\mu m$

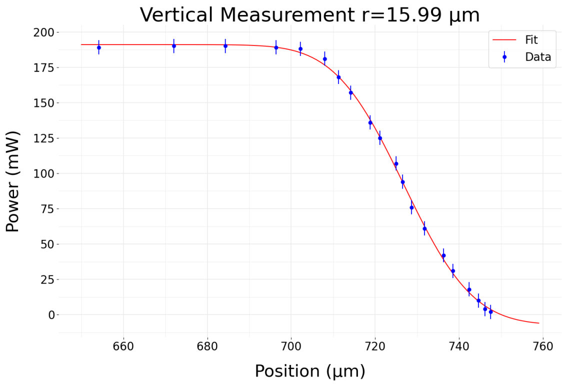

Fig. A.51: $x = 190.3\mu m$, $\sigma = 12.96 \pm 0.33\mu m$

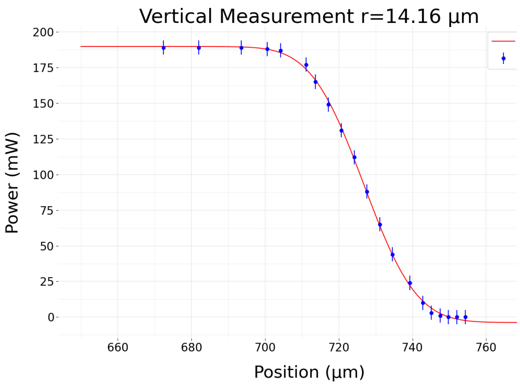

Fig. A.52: $x = 200.6\mu m$, $\sigma = 11.27 \pm 0.17\mu m$

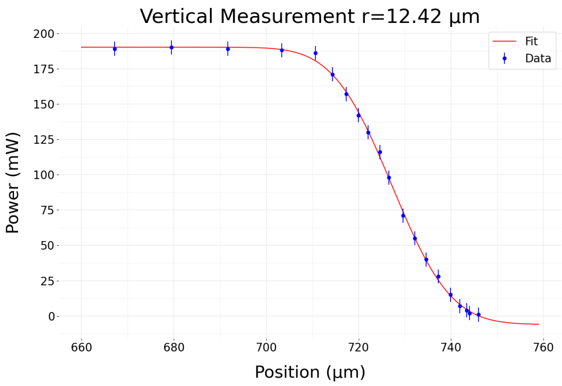

Fig. A.53: $x = 210.75\mu m$, $\sigma = 10.03 \pm 0.20\mu m$

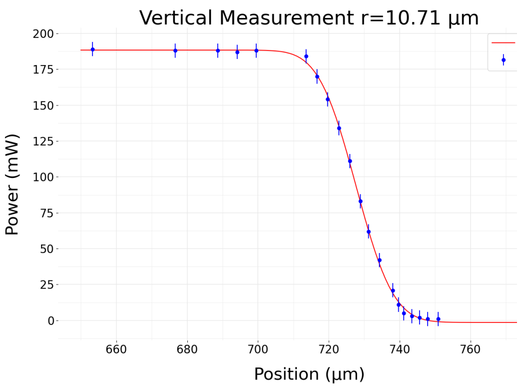

Fig. A.54: $x = 220.8\mu m$, $\sigma = 8.33 \pm 0.13\mu m$

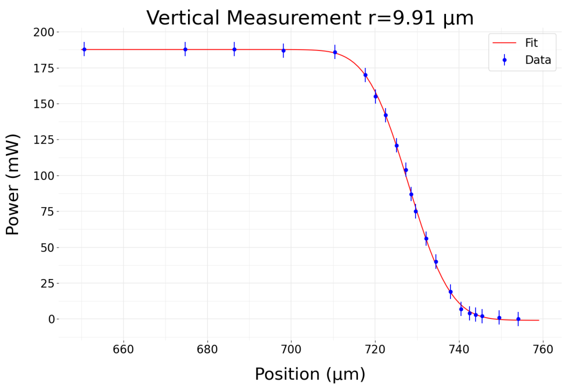

Fig. A.55: $x = 225.3\mu m$, $\sigma = 7.88 \pm 0.10\mu m$

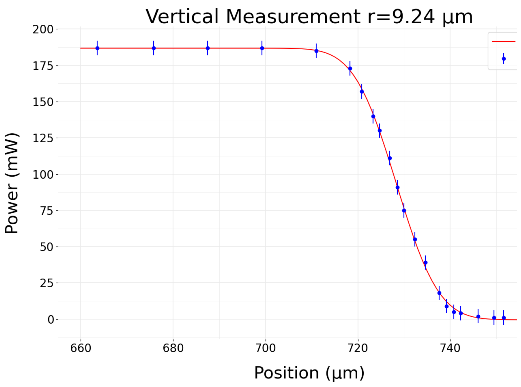

Fig. A.56: $x = 230.3\mu m$, $\sigma = 7.22 \pm 0.099\mu m$

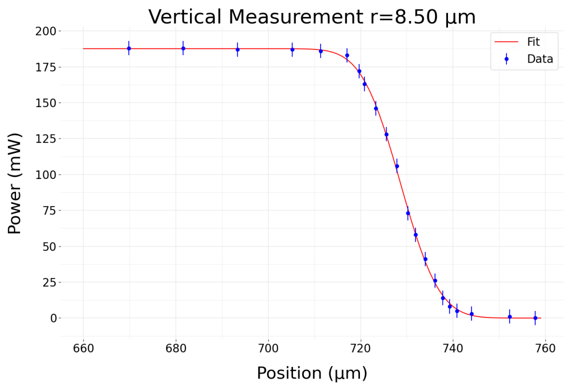

Fig. A.57: $x = 240.6\mu m$, $\sigma = 6.11 \pm 0.08\mu m$

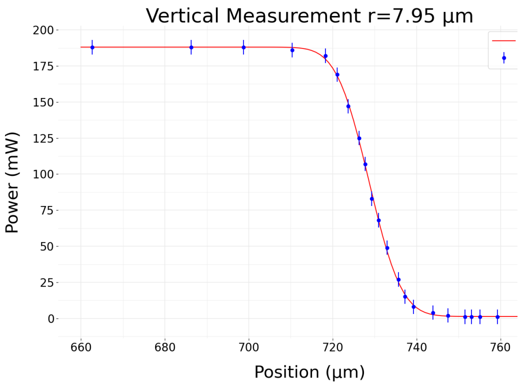

Fig. A.58: $x = 245.8\mu m$, $\sigma = 5.86 \pm 0.06\mu m$

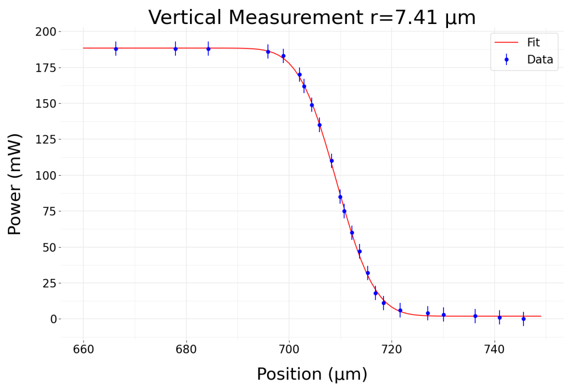

Fig. A.59: $x = 250.3\mu m$, $\sigma = 5.257 \pm 0.0802\mu m$

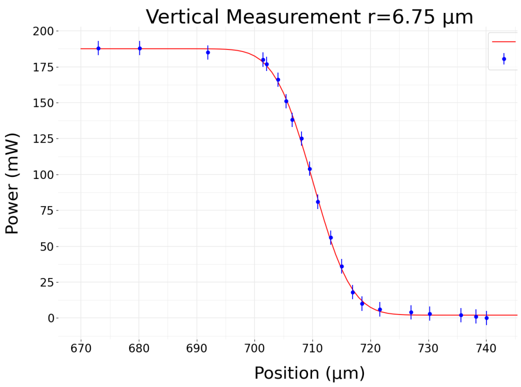

Fig. A.60: $x = 255.4\mu m$, $\sigma = 4.78 \pm 0.06\mu m$

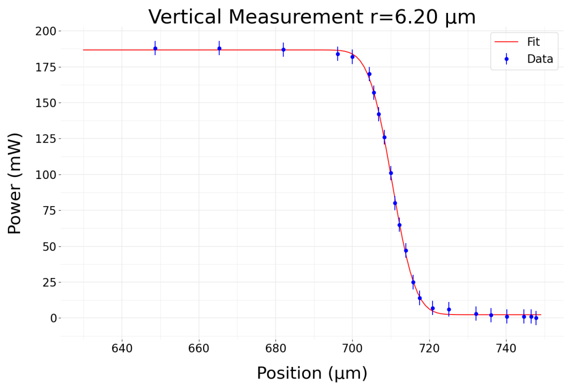

Fig. A.61: $x = 260.1\mu m$, $\sigma = 4.43 \pm 0.07\mu m$

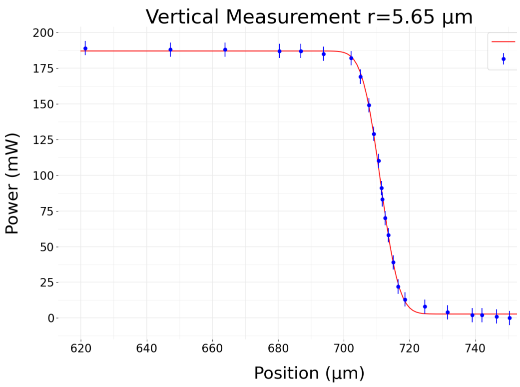

Fig. A.62: $x = 265.6\mu m$, $\sigma = 3.82 \pm 0.068\mu m$

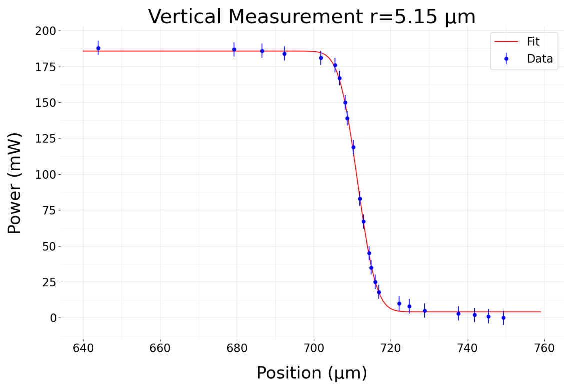

Fig. A.63: $x = 270.1\mu m$, $\sigma = 3.42 \pm 0.07\mu m$

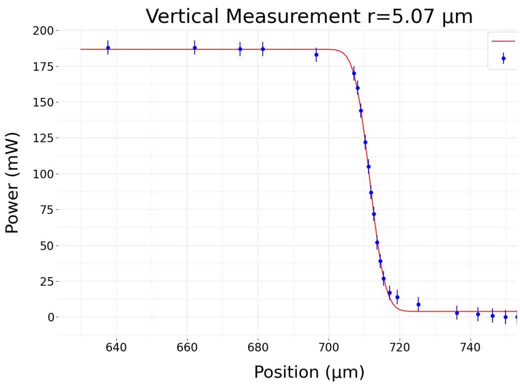

Fig. A.64: $x = 275.3\mu m$, $\sigma = 3.49 \pm 0.11\mu m$

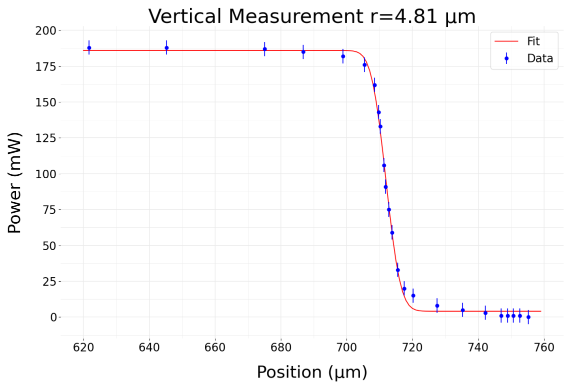

Fig. A.65: $x = 280.4\mu m$, $\sigma = 3.96 \pm 0.12\mu m$

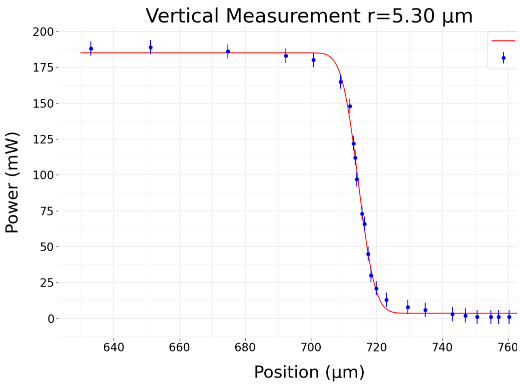

Fig. A.66: $x = 285.6\mu m$, $\sigma = 5.77 \pm 0.15\mu m$

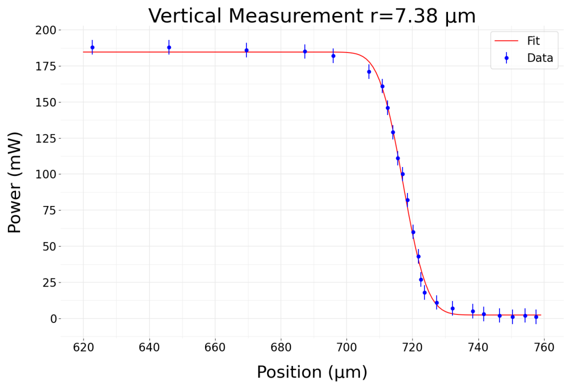

Fig. A.67: $x = 290.8\mu m$, $\sigma = 6.12 \pm 0.23\mu m$

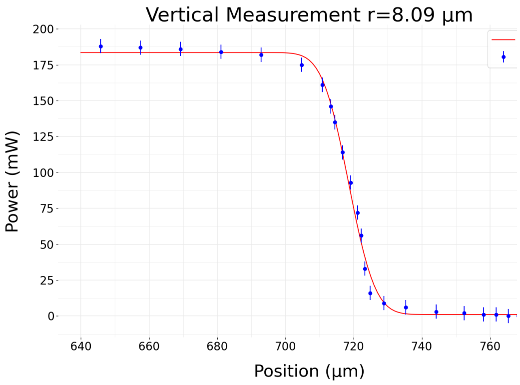

Fig. A.68: $x = 300.8\mu m$, $\sigma = 7.08 \pm 0.39\mu m$

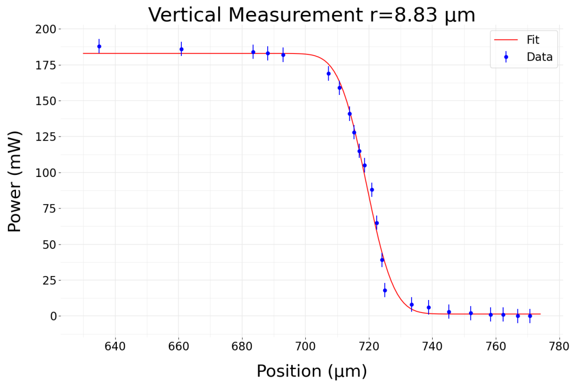

Fig. A.69: $x = 310.4\mu m$, $\sigma = 7.71 \pm 0.27\mu m$

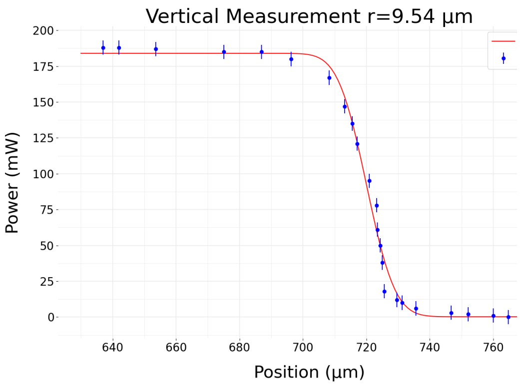

Fig. A.70: $x = 320.7\mu m$, $\sigma = 8.37 \pm 0.26\mu m$

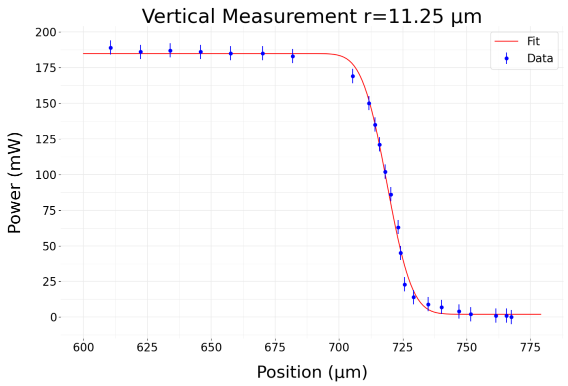

Fig. A.71: $x = 330.7\mu m$, $\sigma = 9.21 \pm 0.29\mu m$

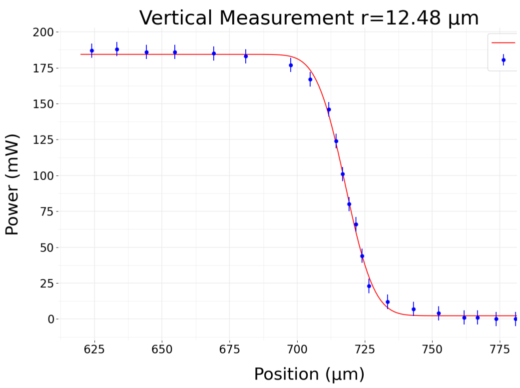

Fig. A.72: $x = 340.6\mu m$, $\sigma = 10.21 \pm 0.36\mu m$

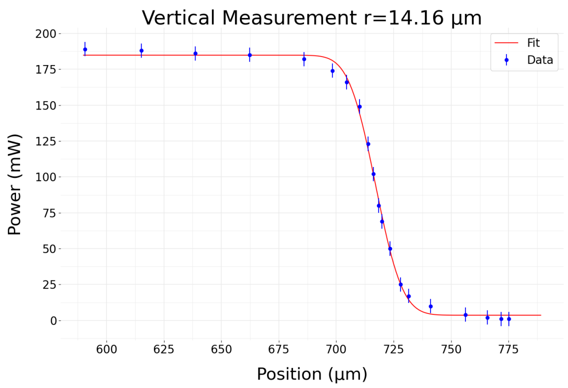

Fig. A.73: $x = 350.3\mu m$, $\sigma = 8.99 \pm 0.53\mu m$

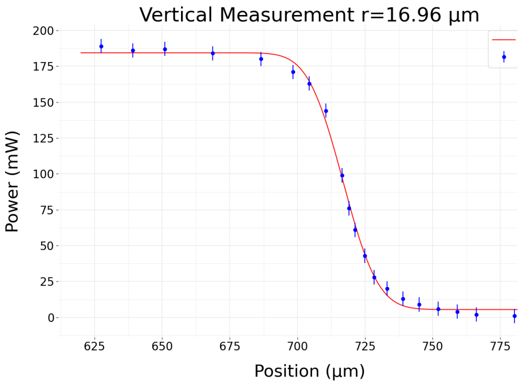

Fig. A.74: $x = 360.6\mu m$, $\sigma = 12.71 \pm 0.37\mu m$

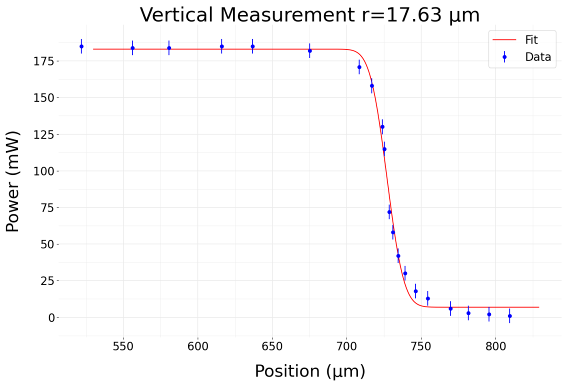

Fig. A.75: $x = 380.9\mu m$, $\sigma = 13.05 \pm 0.53\mu m$

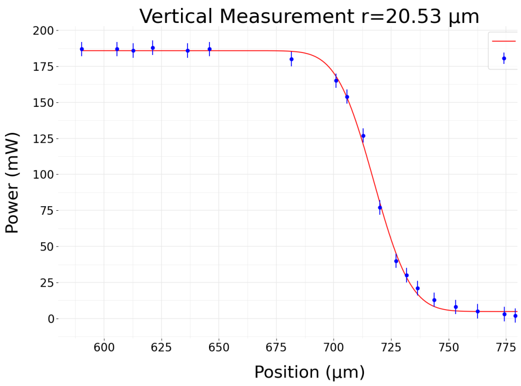

Fig. A.76: $x = 400.6\mu m$, $\sigma = 16.65 \pm 0.50\mu m$

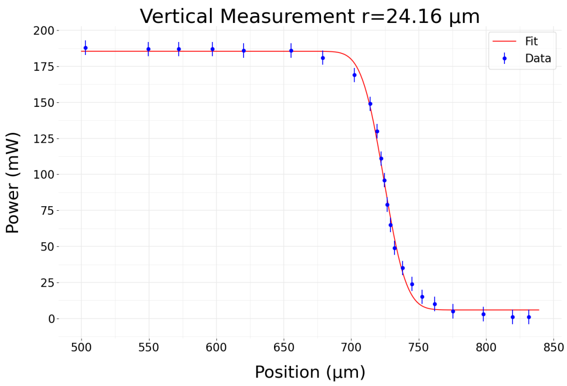

Fig. A.77: $x = 420.5\mu m$, $\sigma = 20.49 \pm 0.54\mu m$

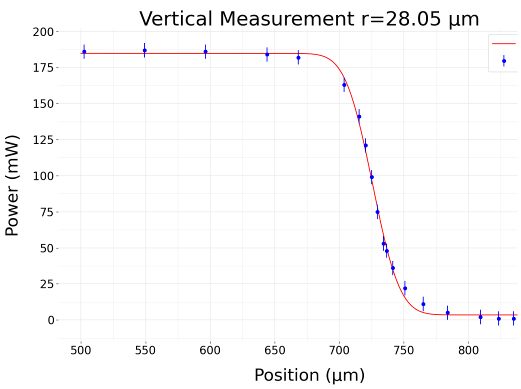

Fig. A.78: $x = 440.1\mu m$, $\sigma = 24.33 \pm 0.58\mu m$

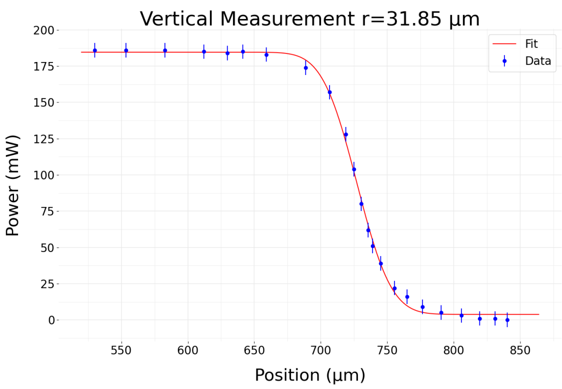

Fig. A.79: $x = 460.2\mu m$, $\sigma = 27.46 \pm 0.58\mu m$

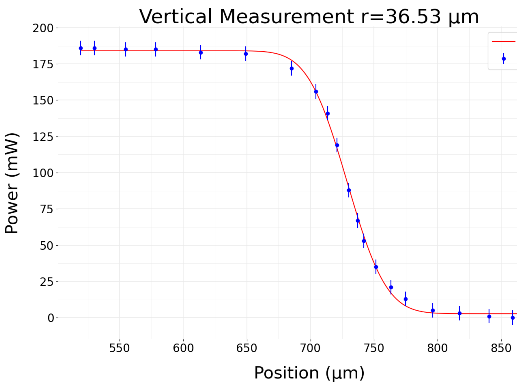

Fig. A.80: $x = 480.4\mu m$, $\sigma = 31.15 \pm 0.63\mu m$

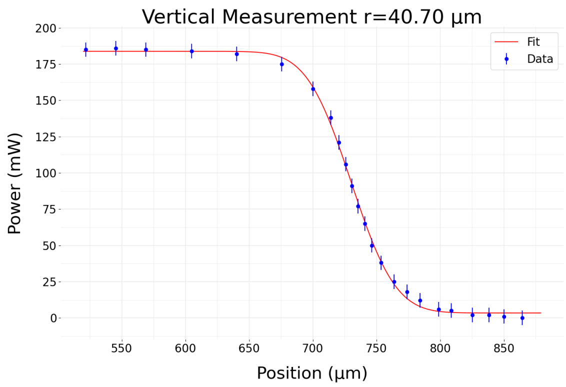

Fig. A.81: $x = 500.8\mu m$, $\sigma = 33.68 \pm 0.53\mu m$

Bibliography

[1] Mack, Chris A. "Optical Lithography." Bellingham: SPIE Field Guides (2006).

[2] Jones, Philip H., Onofrio M. Maragò, and Giovanni Volpe. Optical tweezers: Principles and applications. Cambridge University Press, 2015.

[3] Tassieri, Manlio, ed. Microrheology with Optical Tweezers: Principles and Applications. CRC Press, 2016.

[4] Ashkin, Arthur. "Optical trapping and manipulation of neutral particles using lasers." Proceedings of the National Academy of Sciences 94, no. 10 (1997): 4853-4860.

[5] Bonnett Del Alamo, M., C. Soncco, R. Helaconde, J. L. Bazo Alba, and A. M. Gago. "Laser spot measurement using simple devices." AIP Advances 11, no. 7 (2021): 075016.

[6] Erdmund, "Testing and targets," `https://www.edmundoptics.com/knowledge-center/application-notes/imaging/testing-and-targets/`.

[7] Alexander Franzen, "Component library," `http://www.gwoptics.org/ComponentLibrary/`.

[8] Demtröder, Wolfgang. Experimentalphysik 2: Elektrizität und Optik. Springer-Verlag, 2018.

[9] JGU Mainz, "CLight propagation in dipolar media," `https://www.qoqi.physik.uni-mainz.de/research-projects/dysprosium/`.

[10] J. Eichler, L. D unkel, and B. Eppich, Die Strahlqualit at von Lasern. Wie bestimmt man Beugungsmaßzahl und Strahldurchmesser in der Praxis?, Laser Technik Journal (2004). DOI: 10.1002/latj.200790019